Journal of Petroleum Science and Engineering 215 (2022) 110393

Contents lists available at ScienceDirect

Journal of Petroleum Science and Engineering

journal homepage: www.elsevier.com/locate/petrol

Stimulating relative permeability changes by low-frequency elastic waves: Theory and lab experiments

Alexander Y. Rozhko [a,*], Serhii Lozovyi [b], Marcel Naumann [a], Fredrik Hansteen [a], Matteo Ravasi [c]

[a] Equinor ASA, Norway
[b] SINTEF, Norway
[c] King Abdullah University of Science and Technology, Saudi Arabia

ARTICLE INFO

Keywords:
Multiphase flow
Stimulation
Elastic waves
Low-frequency
Contact angle hysteresis
Partial saturation

ABSTRACT

A model is presented to describe how low-frequency vibrations can induce changes to relative permeabilities in dual-porosity dual-permeability rocks. We show that a combination of two physical processes may cause this effect: 1) the wave-induced two-phase fluid flow between soft pores (fractures or cracks) and stiff pores (matrix); and 2) the contact angle hysteresis effect. These two effects lead to redistribution of fluid saturation between fractures and matrix, which may explain alteration of relative permeabilities by small transient strains ($\sim 10^{-6}$) in rocks where the fluid flow occurs primarily through the fracture network, and fluid storage occurs predominantly in the porous matrix. We assume that the frequency is low enough that viscous and inertial effects are negligible and that any stress-induced increments of pore pressure are uniform within wetting and nonwetting fluid phases. We demonstrate that pulse-like vibrations are much more efficient in changing relative permeabilities than sinusoidal-shaped vibrations. Furthermore, we show that two waveforms with the same amplitude and frequency but with different polarities could have opposite effects on the alteration of relative permeabilities. Specifically, extensional pulses increase oil relative permeability and decrease water relative permeability in the water-wet rock. Contrary, compressional pulses decrease oil relative permeability and increase water relative permeability in the water-wet rock. To validate theoretical results, we developed a unique low-frequency laboratory setup and experimental methods. We performed drainage and imbibition cycles on a sandstone sample using oil and water as pore fluids. During flooding, the sample was excited by small-strain seismic pulses of a specific shape, with varying polarization direction, frequency, and amplitude. The preliminary laboratory results validate the theoretical model qualitatively. The proposed model may contribute to environmentally friendly and low-cost methods for stimulating hydrocarbon production in conventional reservoirs without invasive chemicals or fracking. In unconventional reservoirs, however, this technology can be envisioned as supplementary to standard EOR/IOR techniques. Normally, the seismic wave energy is too low to increase absolute permeability or decrease oil viscosity; only relative permeabilities can be affected.

1. Introduction

Improving multiphase flow in porous media is of concern for many practical applications, including stimulating hydrocarbon production, geological storage of carbon dioxide, and ground-water management. Laboratory, field, and theoretical studies have shown that the propagation of elastic waves can change the multiphase flow and transport properties of porous media (e.g., Beresnev and Johnson, 1994; Roberts et al., 2003; Manga et al., 2012; Shi et al., 2015). Experimental observations indicate that low-frequency (<100 Hz) seismic waves, such as those created by distant earthquakes and anthropogenic noise, may significantly affect the water and oil production, increase discharge in streams and springs, and change the water level in wells. These effects are observed even at hundreds of kilometers from earthquakes hypocentres (e.g., Beresnev and Johnson, 1994; Nikolaevskiy et al., 1996; Kouznetsov et al., 1998; Roberts et al., 2003; Manga et al., 2012; Shi et al., 2015). However, at these distances, the amplitudes of dynamic stresses are very small, ~0.1 bars (dynamic strain $\sim 10^{-6}$); therefore, it is challenging to explain these effects theoretically.

Published field data show that elastic waves can positively or negatively affect multiphase fluid flow in porous media. The oil-water ratio in producing wells can either increase or decrease if the reservoir is

* Corresponding author.
E-mail address: arozh@equinor.com (A.Y. Rozhko).

https://doi.org/10.1016/j.petrol.2022.110393
Received 29 November 2021; Received in revised form 5 March 2022; Accepted 10 March 2022
Available online 28 March 2022

subjected to elastic waves (Beresnev and Johnson, 1994; Nikolaevskiy et al., 1996; Manga et al., 2012). Also, water-level in wells can either increase or decrease (e.g., Manga et al., 2012; Shi et al., 2015). The positive and negative effects of transient stresses on rock permeability were also observed in the lab (Shmonov et al., 1999; Roberts et al., 2003; Liu and Manga, 2009; Elkhoury et al., 2011; Boeut, 2020). The data review of Manga et al. (2012) shows that a few cycles of dynamic excitations are enough to induce the observed changes in flow behavior. Both field and lab data show that upon stopping the dynamic excitations, the oil mobility recovers to prestimulated values with a typical time-scale, which varies from minutes in the lab to months in the field (Beresnev and Johnson, 1994; Nikolaevskiy et al., 1996; Manga et al., 2012; Boeut, 2020). Manga et al. (2012) argued that the relaxation of fluid mobilities to prestimulated values behaves exponentially with time. The observed recovery time is longer for larger transient stress amplitudes (Boeut, 2020). Manga et al. (2012) claimed that there is a threshold in terms of wave amplitude for a hydraulic response. If the wave amplitude is smaller than a threshold value, the elastic wave does not affect the multiphase fluid flow; however, when the wave amplitude is larger than its critical value, the increase in permeability is scaled exponentially with wave amplitude (Manga et al., 2012 and references therein).

Theoretically, the effect of small seismic waves (or transient stresses) on alteration of fluid mobilities have been studied extensively in the literature (e.g., Surguchev et al., 1975; Beresnev and Johnson, 1994; Nikolaevskiy et al., 1996; Kouznetsov et al., 1998; Pride et al., 2008; Roberts and Abdel-Fattah, 2009; Manga et al., 2012; Mirzaei-Paiaman and Nourani, 2012; Candela et al., 2014; Shi et al., 2015; Taira et al., 2018; Barbosa et al., 2019; Zeng et al., 2020a, 2020b). The suggested models can be divided into two classes of processes that can explain how small changes in stress could change permeability: 1) mobilization of colloidal deposits and 2) mobilization of pore-blocking or fracture-blocking nonwetting bubbles or droplets. Previous authors argued that the resonances of oil drops could cause the wave-induced mobilization of oil drops at the pore scale (Beresnev, 2006; Hilpert, 2007; Frehner et al., 2009; Holzner et al., 2009; Zeng et al., 2020a, 2020b). Recently, Zeng et al. (2020a, 2020b) and Al-Shami et al. (2021) investigated resonances of oil drops in constricted capillary tubes. However, the authors neglected the elastic deformation of constricted tubes. Thus, it is unclear how to apply their model to explain changes of relative permeability in deformable pores during elastic wave propagation (Rozhko, 2020a). A detailed literature review of different models at seismic frequencies can be found in Manga et al. (2012), Jeong et al. (2015), and Barbosa et al. (2019).

Despite a comprehensive literature list, current theoretical models cannot adequately answer the following questions:

1. Why and when can small seismic waves either increase or decrease hydrocarbon mobility? Possible explanations suggest that these effects are controlled by wave-induced unclogging or clogging of pore throats or fractures by colloidal deposits, such as fines or nonwetting bubbles or droplets (Manga et al., 2012; Barbosa et al., 2019). When will hydrocarbon mobility change? What controls the positive or negative effects on multiphase fluid flow?
2. What is the critical wave amplitude required for the alteration of hydrocarbon production? How much will the phases' permeabilities change when the wave amplitude is larger than its threshold value?
3. What controls the relaxation of phase permeabilities to prestimulated values? Some scholars argue that the recovery mechanism is related to clogging of pore throats (e.g., Manga et al., 2012) or of fractures (e.g., Barbosa et al., 2019). Why is it thermodynamically favorable for multiphase permeabilities to recover to prestimulated value? What controls the kinematics of permeability relaxation?

This paper presents a new model, which offers a possible explanation to the above questions. Our new model is based on contact angle hysteresis modeling (CAH) in the deformable crack during wave-induced two-phase fluid flow between the crack and the rock matrix. The CAH was not discussed in the literature review cited above; however, recent studies show that CAH is deemed to be very important for understanding multiphase fluid flow in porous media (Blunt, 2017; Blunt et al., 2019; Scanziani et al., 2020; Mascini et al., 2020; Sun et al., 2020b). Therefore, we apply the CAH concept to better understand the alteration of relative permeabilities by elastic waves. Furthermore, we utilize the concept of the most stable contact angle (e.g., Drelich, 2019). We demonstrate that the relaxation of relative permeabilities to prestimulated values is driven by the relaxation of contact angles to the most stable configuration.

Our model assumes that the frequency is low enough that viscous forces are negligible and that any stress-induced increments of pore pressure are uniform within each fluid phase. However, the pore pressure increments are different for the wetting and non-wetting fluid phases due to capillary pressure and different compressibilities of pore fluids. It needs to be mentioned that this assumption of neglecting viscosity is commonly used in Gassmann's theories, developed for seismic velocity modeling (e.g., Gassmann, 1951; Mavko et al., 2020). It implies that deformation and wave-induced fluid flow are quasi-static. If the frequency is not low enough, it will not be sufficient time for fluids to flow between fracture and matrix and re-distribute the saturation. Thus, this high-frequency wave will be less efficient in stimulating relative permeabilities by the suggested mechanism. This assumption seems to be supported by field observations. Manga et al. (2012) argue that the current field evidence favours long-period waves as being more effective at increasing permeability for a given wave amplitude than short-period waves. Based on numerical modeling, Zare et al. (2021) also concluded that the mobilization of gas, sitting in the rock matrix, into fractures is more efficient at lower frequencies. It is also important to note that changes in fluid mobility are also observed at ultrasonic frequencies (e.g., Mullakaev et al., 2019; Mat-Shayuti et al., 2019; Khasi et al., 2021). However, underlying mechanisms that lead to the enhancement of fluid mobility are different at such frequencies. The mechanisms here include viscosity and interfacial tension reduction due to heating caused by the attenuation of ultrasonic waves, the collapse of interfacial films between the immiscible fluids, resonances, and the coalescence of oil droplets (Mullakaev et al., 2019; Mat-Shayuti et al., 2019). It is more challenging to explain these effects at seismic frequencies. Here, heating effects are negligibly small; also, the resonances are not possible in this frequency range in reservoir rock (Broadhead, 2010).

Although our model suggests possible explanations to the above three questions, this pore-scale model does not provide a complete explanation of wave-induced changes of relative permeabilities in reservoir rocks. There, the crack (fracture) porosity can be a small fraction of total porosity, while the crack permeability can significantly affect the total permeability of dual-porosity rocks. Therefore, fluid flow may occur primarily through the fracture network, but fluid storage may occur mainly in the porous matrix (e.g., Barenblatt et al., 1990; Berryman and Wang, 1995; Pouya et al., 2013). The total permeability of the matrix and cracks system is the most challenging property to define because it is highly heterogeneous, anisotropic, and dependent on the flow boundary conditions. This paper simplifies the problem and considers only an isolated crack (or fracture) surrounded by a porous medium with effective elastic properties: Young's modulus, Poisson's ratio, and two Skempton's B coefficients (defined below) for the wetting and nonwetting fluid phases. These properties may, of course, depend on the fluid saturation of the matrix, but we do not consider this dependence at this stage. Additionally, we assume that matrix and crack are hydraulically connected, meaning that two-phase fluids can flow between them to eliminate the wave-induced gradients of pore pressure in each phase. Thus, our pore-scale model explains changes of relative permeabilities only in the isolated crack and only in the low-frequency limit.

This paper is constructed as follows. First, we introduce some necessary theoretical background, such as the contact angle hysteresis

and the most stable contact angle concepts. Next, we derive equations for pore-scale modeling of changes in relative permeabilities induced by elastic waves. Thereafter, we present numerical examples of the effect of input parameters, wave amplitudes, and waveform shapes on the stimulation of relative permeabilities. Further, we describe the first laboratory validation test on a sandstone sample. We then discuss the results and conclude the paper. Finally, the manuscript includes MATLAB code, which can be used to reproduce the results claimed in the paper, for further investigation of the model's input parameters, or for a better understanding of the mathematical modeling. The manuscript is also supported by a report with the laboratory experimental results.

2. Theory

2.1. Contact angle hysteresis

The contact angle of the liquid droplet deposited on the solid surface is defined uniquely by the Young equation (Young, 1805):

$$\theta_Y = \frac{\gamma_{SA} - \gamma_{SL}}{\gamma} \tag{1}$$

where γ_{SA}, γ_{SL}, and γ are the surface tensions at the solid/air, solid/liquid, and liquid/air interfaces, respectively. However, a spectrum of static contact angles is observed. This phenomenon is called contact angle hysteresis. The highest possible contact angle that can be achieved for a given wetting system is called the advancing contact angle θ_a, whereas the lowest possible contact angle is called the receding contact angle θ_r. The pore/crack surface roughness and chemical and mineralogical heterogeneities contribute substantially to the contact angle hysteresis in porous materials. The origin of the contact angle hysteresis is related to the pinning of the triple (three-phase) line by physical or chemical heterogeneities of the substrate (Bormashenko, 2013; Drelich, 2019). The contact angle hysteresis is also observed on ideal, i.e., atomically smooth, rigid, nonreactive surfaces. It depends on many parameters, including roughness and mineralogical composition of the substrate surface (i.e., pore surface or grain/crack surface), temperature, fluid pressure, and chemical composition of pore fluids (e.g., Bormashenko, 2013; Drelich, 2019; Ali et al., 2020; Ali et al., 2022).

The distribution of contact angles inside porous materials can be obtained based on visual interpretation of synchrotron-based X-ray microtomography images (Andrew et al., 2015; Khishvand et al., 2017); automated algorithms (AlRatrout et al., 2017; Scanziani et al., 2017) or methods based on Gauss-Bonnet theorem establishing a direct link between contact angle and bulk fluid topology (Sun et al., 2020a, 2020b). In addition, the recent literature review by Ali et al. (2021) provides more details on different methods for rock's wettability determination at reservoir conditions.

When a static contact angle is close to advancing or receding, the contact angle is not energetically favorable (Drelich, 2019). A metastable contact angle will relax to the most stable and energetically favorable contact angle (θ_{st}), corresponding to the minimum of Gibb's free energy (Drelich, 2019). The equilibration time, during which the contact angle of the liquid droplet relaxes to a more stable state, can take anywhere from hours to days (Drelich, 2019). Unfortunately, contact angle relaxation measurements are scarce in the technical literature (Drelich, 2019). The most stable and energetically favorable contact angle can be approximated by the mean angle (Drelich, 2019):

$$\theta_{st} = \frac{\theta_a + \theta_r}{2} \tag{2}$$

It needs to be mentioned that there is a discussion in the literature about equation (2), which may not be precise (Bormashenko, 2013; Drelich, 2019). However, for our applications, the exact expression for the most stable contact angle is not essential. The most important is that the most stable contact angle exists and is unique.

The relaxation of the contact angle to the most stable and energetically favorable configuration is governed by an exponential function (e.g., Lee et al., 2008):

$$\cos(\theta) = \cos(\theta_{st}) + (\cos(\theta_0) - \cos(\theta_{st}))\exp\left(-t/\Delta T\right). \tag{3}$$

Here ΔT is the equilibration time, during which the contact angle relaxes to the most stable state, and θ_0 is the contact angle at the zero time. Hither, the relaxation of the contact angle to the most stable and energetically favorable configuration will induce alterations in the wetted area diameter (e.g., Drelich, 1999). This relaxation of the wetted area diameter is driven by the relaxation of the contact angle and conservation of the liquid's drop mass when evaporation is neglected.

Below we assume that the transient stress period during elastic wave propagation in the porous rock is much smaller than the equilibration time ΔT. Therefore, the recovery of the contact angle during stress vibrations can be neglected. In contrast, it is not neglected on a much larger time scale after stopping the dynamic stimulation. We also consider that the initial contact angle (before elastic wave excitations) is equal to the most stable contact angle defined above.

2.2. PORE-SCALE model

To model the effect of elastic wave excitation on relative permeabilities of the partially saturated crack, we approximate the crack geometry by an elliptical cavity and use a plane-strain (2D) approximation. These approximations are widely employed in effective medium theories (e.g., Mavko et al., 2020). Fig. 1a shows a representative elementary volume (REV) with a partially saturated crack. We model two-phase permeabilities of an elliptical crack in the z-direction perpendicular to the plane of Fig. 1a. In contrast, the wave-induced two-phase fluid flow between the crack and matrix are along the in-plane directions x and y.

Here we consider water as the wetting phase and oil (or gas) as the non-wetting phase. The nonwetting phase at pressure p_{nw}occupies the central part of the elliptical cavity, with $|x| \le c$. In contrast, the wetting phase at pressure p_{we} occupies the tips with $c \le |x| \le a$. Here, $|x| = c$ denotes the contact line's location, also known as the triple line. The initial geometry of the elliptical cavity at zero effective stress is defined by major and minor semi-axes, as a and b. We consider a very thin cavity, i.e., a crack with $a \gg b$. The contact angle made by the wetting phase is θ. A porous and permeable medium surrounds the crack with effective elastic properties, defined above. The two-phase fluid can flow between the crack and matrix to eliminate gradients of fluid pressure. The conditions on the external boundary of the representative elementary volume are defined by the total uniform stress σ, fluid pressure in the wetting phase p_{we}, and fluid pressure in the nonwetting phase p_{nw}. Since we neglect the viscosity and inertia terms, we consider a uniform fluid pressure in each fluid phase within a REV, shown in Fig. 1a.

The capillary pressure is defined as:

$$p_{cap} = p_{nw} - p_{we}. \tag{4}$$

Fig. 1b shows the wave-induced perturbation of the equilibrium state. The elastic wave-stress increment $\delta\sigma$ induces changes to pressure in the wetting δp_{we}, and nonwetting δp_{nw} phases. As we already discussed, our model assumes that the frequency is low enough and that any stress-induced increments of pore pressure are uniform within each fluid phase within a representative elementary volume. However, the pore pressure increments are different for the wetting and nonwetting fluid phases, as defined below. Elastic wave induces the deformation of the elliptical crack, which affects the contact angle $\delta\theta$ and the location of the contact line δc inside the crack (Fig. 1b).

Below we calculate wave-induced changes in relative permeabilities in two successive steps. First, we calculate relative permeabilities at the equilibrium state (Fig. 1a). And second, we define a quasi-static perturbation of the equilibrium state by a wave-stress increment (Fig. 1b). The successive computations are performed until the response of the whole waveform is obtained. The last subsection of this section

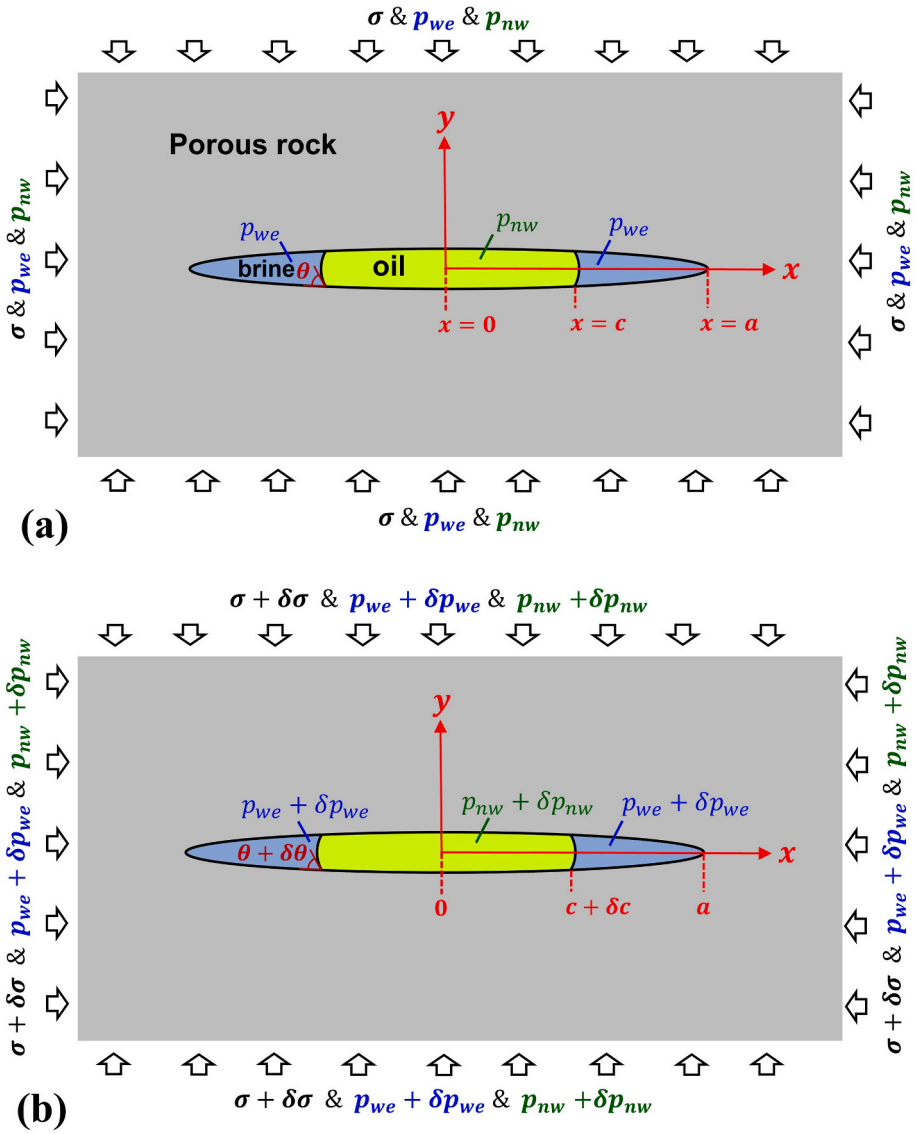

Fig. 1. Representative elementary volume (REV) with a partially saturated plane-strain crack. Two-phase crack's permeabilities are modeled in **z** – direction, perpendicular to the plane of the figure. Fig. 1a shows the equilibrium state, while Fig. 1b shows wave-induced quasi-equilibrium perturbation of the equilibrium state in the low-frequency limit. The wave-induced two-phase fluid flow between the crack and matrix is considered in-plane directions.

explains how to relate the wave-stress increment to the wave-strain increment.

2.2.1. Relative permeabilities in the equilibrium state

To calculate the relative permeabilities of a partially saturated crack, first, we need to define how the location of the contact line inside the crack is related to the capillary pressure. Second, we need to define the aperture of a partially saturated crack and relate it to the crack's relative permeabilities and saturation degree.

The capillary pressure affects the deformation of the elliptical crack. The half aperture of the elliptical crack is calculated as follows (Rozhko, 2016):

$$\frac{w_\vartheta}{b}=\left(p_{cl}+\sigma+p_{we}+\left(1-\frac{2\beta}{\pi}\right)p_{cap}\right)\frac{\sin(\vartheta)}{p_{cl}} -\frac{p_{cap}}{\pi p_{cl}}\left(\cos(\vartheta)\ln\frac{\sin(\beta+\vartheta)}{\sin|\beta-\vartheta|}+\cos(\beta)\ln\frac{|\sin(\beta)-\sin(\vartheta)|}{\sin(\beta)+\sin(\vartheta)}\right) \quad (5)$$

Here p_{cl} is the crack closure pressure (Rozhko, 2016):

$$p_{cl}=\frac{bE}{2a(1-\nu^2)}; \quad (6)$$

E and ν are effective Young's modulus and Poisson's ratio of the porous rock around the elliptical crack; the angle ϑ defines the distance from the crack center along the crack tip direction (x coordinate) as follows (Rozhko, 2016):

$$x=a\bullet\cos(\vartheta); \quad (7)$$

the angle β defines the location of the contact line (Fig. 1a):

$$c=a\bullet\cos(\beta). \quad (8)$$

The location of the contact line is yet an unknown parameter in equation (5). This parameter is calculated by coupling the capillary pressure to the crack aperture deformation (Rozhko, 2016). Indeed, equation (5) gives the following expression for half crack's aperture at the contact line location when $\vartheta=\beta$ (or equivalently, when $x=c$):

$$w_\beta=\frac{b}{p_{cl}}\left(p_{cl}+\sigma+p_{we}+p_{cap}\frac{\pi-2\beta-2\cot(\beta)\ln(\cos(\beta))}{\pi}\right)\sin(\beta). \quad (9)$$

From equation (9), we see that half aperture of the elliptical cavity at the contact line location (w_β) depends on the capillary pressure. At the same time, the capillary pressure (in 2D) depends on w_β according to Laplace equation as follows (Rozhko, 2016):

$$p_{cap} = \frac{\gamma \cos(\theta)}{w_\beta} \tag{10}$$

Here γ is the interfacial tension between immiscible fluids, while the contact angle θ is defined for the wetting phase. Equations (9) and (10) give the quadratic equation on the capillary pressure. The physically meaningful solution to this quadratic equation is

$$p_{cap} = \frac{\pi}{4}(p_{cl} + \sigma + p_{we}) \frac{1 - \sqrt{1 - \frac{8}{\pi} p_{cl} \frac{\gamma \cos(\theta)}{b} \frac{(\beta + \cot(\beta)\ln[\cos(\beta)] - \pi/2)}{(p_{cl} + \sigma + p_{we})^2 \sin(\beta)}}}{\beta + \cot(\beta)\ln[\cos(\beta)] - \pi/2} \tag{11}$$

Indeed, when the interfacial tension is equal to zero, equation (11) gives a zero-capillary pressure, as expected. In comparison, the second solution of the quadratic equation (not shown here) gives $p_{cap} \neq 0$ when $\gamma = 0$, which is physically meaningless. The contact line's location (β) is defined by solving equation (11) numerically in a MATLAB code (see supplement).

It should be mentioned that we use a sign convention where compressive stress, strain, and displacement are negative, while compressive pressure is positive. Using equation (5), we can calculate the volume of the deformed elliptical cavity by integrating the cavity aperture along the cavity length (i.e., $V_{cr} = 4a \int_0^{\pi/2} w_\vartheta \sin(\vartheta) d\vartheta$) as follows (Rozhko, 2016):

$$\frac{V_{cr}}{\pi a b} = 1 + \frac{\sigma_\perp + p_{we} + \left(1 + \frac{\sin(2\beta) - 2\beta}{\pi}\right) p_{cap}}{p_{cl}} \tag{12}$$

The volume of the wetting phase inside the cavity is calculated by integrating the cavity aperture along the length occupied by the wetting phase, i.e. $V_{we.1} = 4a \int_0^{\beta} w_\vartheta \sin(\vartheta) d\vartheta$ as follows:

$$\frac{V_{we.1}}{\pi a b} = \left(1 + \frac{\sigma + p_{we} + p_{cap}\left(1 + \frac{4}{\pi}\left[\frac{\beta \sin(2\beta) - \beta^2 + 2\cos^2(\beta)\ln[\cos(\beta)]}{2\beta - \sin(2\beta)}\right]\right)}{p_{cl}}\right) \frac{(2\beta - \sin(2\beta))}{\pi} \tag{13}$$

The calculation in equation (13) does not consider the curvature of the interface meniscus. This additional volume due to meniscus curvature is calculated as follows (Rozhko, 2019):

$$V_{we.2} = -\frac{(\pi - 2\theta - \sin(2\theta))}{\cos^2(\theta)} w_\beta^2. \tag{14}$$

Thus, the total volume of the nonwetting phase is calculated as follows:

$$V_{we} = V_{we.1} + V_{we.2} \tag{15}$$

This additional volume due to curvature of interface meniscus ($V_{we.2}$) is extremely small ($V_{we.2} \ll V_{we.1}$), because $b \ll a$. And thus, this correction can be neglected during crack saturation and relative permeability calculations.

Here, water phase saturation of the crack, (S_{we}), is defined as:

$$S_{we} = \frac{V_{we}}{V_{cr}} \tag{16}$$

Note here that equations (12)–(15) define the volume in two dimensions: the volume per unit length along the direction perpendicular to the plane of Fig. 1a. Finally, relative permeabilities of the elliptical crack along the direction perpendicular to the plane of Fig. 1a are calculated as follows (see details in Rozhko, 2016). The relative permeability for the wetting phase is calculated as

$$k_{r.we} = \frac{\int_0^{\beta} w_\vartheta^3 \sin(\vartheta) d\vartheta}{\int_0^{\pi/2} w_0^3 \sin(\vartheta) d\vartheta}, \tag{17}$$

and the relative permeability for the nonwetting phase is calculated as

$$k_{r.nw} = \frac{\int_\beta^{\pi/2} w_\vartheta^3 \sin(\vartheta) d\vartheta}{\int_0^{\pi/2} w_0^3 \sin(\vartheta) d\vartheta}. \tag{18}$$

In the above equations, w_0 defines the aperture of water-saturated crack calculated as follows:

$$w_0 = \frac{b}{p_{cl}}(p_{cl} + \sigma + p_{we}) \sin(\vartheta) \tag{19}$$

Thus, in the above equations, the relative permeabilities are defined relative to the permeability of the water-saturated crack. Furthermore, since we in the following will be considering the wave-induced perturbation of the far-field stress, we will define relative permeabilities relative to the permeability of the water-saturated crack at the initial stress before elastic wave excitation.

2.2.2. *Wave-induced perturbation of relative permeabilities*

In this subsection, we develop equations to calculate the stress-vibration effect on the relative permeabilities of a partially saturated crack. Following previous scholars, we calculate the wave-induced increments of pore pressure in the wetting and nonwetting phases, which are related to the wave-stress increment via two Skempton's poroelastic coefficients (B_{we} and B_{nw}) (Skempton, 1954; Pride et al., 2004; Lu and Hanyga, 2005; Müller et al., 2010; Masson and Pride, 2011; Rozhko, 2020b):

$$\delta p_{we} = -B_{we} \delta\sigma, \tag{20}$$

and

$$\delta p_{nw} = -B_{nw} \delta\sigma. \tag{21}$$

Papageorgiou et al. (2016) discussed experimental data, showing that increments of δp_{we} and δp_{nw} are not identical. Here we remind the reader that compressive stress increments are negative due to our sign convention, while compressive pressure increments are positive; therefore, we have a minus sign in front of positive Skempton's coefficients in equations (20) and (21). Thus, the wave-induced increment of the capillary pressure is calculated as follows:

$$\delta p_{cap} = \delta p_{nw} - \delta p_{we}. \tag{22}$$

Approaching this from another side, the wave induced increment of capillary pressure can be calculated by linearization of equation (11) as follows:

$$\delta p_{cap} = \frac{\partial p_{cap}}{\partial \sigma} \delta\sigma + \frac{\partial p_{cap}}{\partial p_{we}} \delta p_{we} + \frac{\partial p_{cap}}{\partial \theta} \delta\theta + \frac{\partial p_{cap}}{\partial \beta} \delta\beta, \tag{23}$$

During Taylor's expansion of equation (11), we keep only linear terms (in equation (23)) because the higher-order terms are negligibly small for sufficiently small wave-stress increment $\delta\sigma$. Note here that the wave-stress increment is not the same as the wave-stress amplitude $\Delta\sigma$. A low-frequency wave of arbitrary waveform can be discretized as much smaller wave-stress increments ($\delta\sigma \ll \Delta\sigma$); therefore, in equation (23), we neglected high-order terms. In equation (23), $\delta\theta$ and $\delta\beta$ are wave-induced changes in the contact angle and the contact line location. According to equation (11), the capillary pressure also depends on other parameters, such as the rock's elastic properties around a crack, interfacial tension, and crack length. We consider that these additional parameters do not change during vibrations; therefore, the increment of the capillary pressure in equation (23) depends only on increments of $\delta\sigma$, δp_{we}, $\delta\theta$, and $\delta\beta$.

Using equations (20)–(22), we can rewrite equation (23) as:

$$\frac{\partial p_{cap}}{\partial \theta}\,\delta\theta+\frac{\partial p_{cap}}{\partial \beta}\,\delta\beta=\left(B_{we}-B_{nw}-\frac{\partial p_{cap}}{\partial \sigma}+B_{we}\frac{\partial p_{cap}}{\partial p_{we}}\right)\delta\sigma. \tag{24}$$

The partial derivatives that appear in the above equations can be found in the Appendix. This equation links two unknown parameters $\delta\theta$ and $\delta\beta$ to the wave-stress increment $\delta\sigma$. The unique solution to equation (24) exists due to a contact angle hysteresis phenomenon because these two unknown parameters $\delta\theta$ and $\delta\beta$ cannot change simultaneously. Indeed, when the contact line is pinned, we have $\delta\beta = 0$, and $\delta\theta$ is calculated from equation (24) as follows:

$$\delta\theta=\delta\sigma\frac{B_{we}-B_{nw}-\frac{\partial p_{cap}}{\partial \sigma}+B_{we}\frac{\partial p_{cap}}{\partial p_{we}}}{\frac{\partial p_{cap}}{\partial \theta}} \tag{25}$$

Here, the contact line is pinned when $\theta_r < \theta < \theta_a$, or when $\theta = \theta_a$ and $\delta\theta < 0$, or when $\theta = \theta_r$ and $\delta\theta > 0$. In all other cases, the contact line is slipping. When the contact line is slipping, the contact angle is equal to advancing or receding angle and thus $\delta\theta = 0$, but changes in the contact line position is calculated from equation (24) as follows:

$$\delta\beta=\delta\sigma\frac{B_{we}-B_{nw}-\frac{\partial p_{cap}}{\partial \sigma}+B_{we}\frac{\partial p_{cap}}{\partial p_{we}}}{\frac{\partial p_{cap}}{\partial \beta}} \tag{26}$$

At this stage, we have calculated wave-induced changes in the contact angle $\delta\theta$ and changes in contact line location $\delta\beta$, which correspond to the vibration-induced increments of total stress $\delta\sigma$. Thus, we have calculated a new quasi-equilibrium configuration of fluid phases inside a partially saturated crack, which is defined by the following parameters: $\sigma = \sigma + \delta\sigma$, $p_{we} = p_{we} + \delta p_{we}$, $p_{nw} = p_{nw} + \delta p_{nw}$, $\theta = \theta + \delta\theta$, and $\beta = \beta + \delta\beta$. These parameters uniquely define relative permeabilities, according to the equations in the previous section. Thus, we can calculate relative permeabilities, which correspond to this new quasi-equilibrium state. Next, we can proceed with calculations until the response of the whole waveform is predicted, i.e., when the contribution from all wave-stress increments of the waveform is calculated (see MATLAB Code in Supporting Materials for details).

Finally, after the passage of the elastic wave, the total stress will return to its initial configuration. According to equations (20) and (21), the pore pressure in the wetting and nonwetting phase will also return to their initial configuration after the passage of elastic waves. However, the contact angle and the contact line location will not immediately return to their initial configuration. At the initial configuration before the elastic-wave excitation, the contact angle is equal to the most stable angle, calculated with equation (2), and the contact line location corresponds to the most stable contact angle configuration. According to equation (3), the contact angle will relax exponentially with time to the most stable and energetically favorable configuration. At the same time, the relaxation of the contact angle will cause changes to the contact line location. Those changes can be calculated by considering $\delta\sigma = 0$ in equation (24) as follows:

$$\delta\beta=\delta\theta\frac{\frac{\partial p_{cap}}{\partial \theta}}{\frac{\partial p_{cap}}{\partial \beta}}. \tag{27}$$

These changes are taking place on a time scale which is much longer than the period of the elastic wave; therefore, the relaxation of the contact angle during elastic wave excitations can be neglected. Finally, relaxation of the contact angle and the contact line location will cause relaxation of relative permeabilities according to the equations of the previous section.

2.2.3. Wave strain in the REV

In the above subsection, we derived equations for the wave-stress increment. However, it is also convenient for practical applications to consider the vibration amplitude in terms of elastic wave strain. For example, typical strain amplitudes during seismic wave propagation are tiny, around 10^{-8} to 10^{-6} (e.g., Pride et al., 2008; Müller et al., 2010). Therefore, it is natural to ask whether the vibration amplitude required to stimulate relative permeabilities is in this range, or whether higher wave energy is required. To answer this, we need to compute the strain in the representative elementary volume (REV). Then, according to Betti's reciprocal theorem (e.g., Walsh, 1965; Rozhko, 2019, 2021), the strain in the REV (ε_{REV}) can be related to the strain in the crack (ε_{cr}), to the porosity of the crack (n_{cr}) at the initial effective stress, and to the strain in the material around a crack ($C\Delta\sigma$) as follows:

$$\varepsilon_{REV} = C\Delta\sigma + n_{cr}\varepsilon_{cr}. \tag{28}$$

Here the strain in the crack is calculated as:

$$\varepsilon_{cr}=\frac{\Delta V_{cr}}{V_{cr}}; \tag{29}$$

and the effective compressibility of the material around a crack is given by:

$$C=\frac{2(1+\nu)(1-2\nu)}{E}. \tag{30}$$

Using the same approach, we can also compute the dissipation of vibration energy due to a contact line friction mechanism (Rozhko, 2019, 2021); however, this is outside of the scope of this paper.

2.3. Numerical results

In this section, we simulate the alteration of relative permeabilities of a partially saturated crack by low-frequency elastic waves using the above equations. These equations are implemented in the MATLAB Code, available via the link below. The input parameters used in the model are listed in Table 1.

We present results for two sets of input parameters, Cases 1 and 2. The sensitivity of different input parameters can be investigated using the provided MATLAB code (see supplement). The poro-elastic parameters are within the range typical for sandstone rocks at reservoir conditions (e.g., Zimmerman, 1990; Mavko et al., 2020), and the interfacial tension is typical for an oil-brine system at reservoir conditions. It is finally worth pointing out that all input parameters in Table 1 are widely used in the literature, although some of them are very difficult to measure. Skempton's coefficients, for example, are combined properties of solid, pore space, and fluids. In the unsaturated case, the constants are functions of the degree of saturation. Thus, measurements and tabulation over a range of saturation are generally not feasible for practical applications (see Cheng (2020) for further discussion). Crack porosity and the aspect ratio of the crack can be estimated from the stress-strain

Table 1
Values of input parameters for Cases 1 and 2.

INPUT PARAMETER	CASE 1	CASE 2
Drained Young's modulus	$E = 30\ GPa$	$E = 32\ GPa$
Drained Poisson's ratio	$\nu = 0.35$	$\nu = 0.3$
Skempton's coefficient for the wetting phase	$B_{we} = 0.5$	$B_{we} = 0.65$
Skempton's coefficient for the nonwetting phase	$B_{nw} = 0.45$	$B_{nw} = 0.5$
Interfacial tension between immiscible fluids	$\gamma = 0.025\ Pa \bullet m$	$\gamma = 0.02\ Pa \bullet m$
Advancing contact angle (for the wetting phase)	$\theta_a = 75^o$	$\theta_a = 30^o$
Receding contact angle (for the wetting phase)	$\theta_r = 65^o$	$\theta_r = 20^o$
Far-field stress (negative in compression)	$\sigma = -50\ MPa$	$\sigma = -60\ MPa$
Pressure in wetting phase	$p_{we} = 30\ MPa$	$p_{we} = 30\ MPa$
Porosity of the crack at the initial effective stress	$n_{cr} = 0.01$	$n_{cr} = 0.01$
Semi major axis of elliptical crack	$a = 10^{-5}\ m$	$a = 10^{-4}\ m$
Semi minor axis of elliptical crack	$b = a/50$	$b = a/40$
Relaxation time for the contact angle (see eq. (3))	$\Delta T = 7\ days$	$\Delta T = 7\ days$

Table 2
Experimental stages during drainage (oil flooding of water-saturated sample).

Stages			Pulse parameters						Production		
Flow rate	Pore volumes (PV) injected	Stage duration	Pulse type	Mean frequency of pulse	Interval between pulses	Axial force amplitude	Stress amplitude	Strain amplitude	Brine volume produced	Cumulative brine volume produced	Brine saturation
[ml/min]	[-]	[h]		[Hz]	[s]	[N]	[bar]	[μm/m]	[ml]	[ml]	[%]
0.1	6.7	48.5	no pulses						11.8	11.8	34.7
			Confining pressure								
0.1	4.6	33.3	Extensional	1	4		0.1		0	11.8	34.7
0.1	4.9	35.6	Compressional	1	4		0.1		0	11.8	34.7
0.1	1.6	11.9	Extensional	1	4		0.25		0	11.8	34.7
0.1	1.8	12.7	Compressional	1	4		0.25		0	11.8	34.7
0.1	3.3	24.2	Extensional	1	4		0.5		0	11.8	34.7
0.1	3.2	23.0	Compressional	1	4		0.5		0	11.8	34.7
0.1	1.0	7.2	no pulses						0	11.8	34.7
0.2	5.5	19.7	no pulses						0	11.8	34.7
0.5	53.0	76.6	no pulses						2.7	14.5	28.5
			Differential stress								
0.5	1.0	1.5	Extensional	30	0.03	25	0.12	2	0	14.5	28.5
0.5	10.7	15.5	Compressional	30	0.03	25	0.12	2	~10^{-4}-10^{-3}	14.5	28.5
0.5	2.0	2.8	Extensional	30	0.03	60	0.30	6	0	14.5	28.5
0.5	1.8	2.6	Compressional	30	0.03	60	0.30	6	~10^{-4}-10^{-3}	14.5	28.5
0.5	0.8	1.2	Extensional	30	0.12	120	0.60	12	~10^{-4}-10^{-3}	14.5	28.5
0.5	3.1	4.5	Compressional	30	0.12	120	0.60	12	~10^{-4}-10^{-3}	14.5	28.5
0.5	9.8	14.1	no pulses						~10^{-4}-10^{-3}	14.5	28.5
0.5	1.2	1.7	Extensional	30	0.03	120	0.60	12	~10^{-4}-10^{-3}	14.5	28.5
0.5	2.9	4.3	Compressional	30	0.03	120	0.60	12	~10^{-4}-10^{-3}	14.5	28.5
0.5	2.2	3.2	Extensional	50	0.07	120	0.60	12	0	14.5	28.5
0.5	3.0	4.4	Compressional	50	0.07	120	0.60	12	0	14.5	28.5
0.5	8.2	11.8	no pulses						0	14.5	28.5
20	465.5	16.8	no pulses						5.8	20.3	15.1

curves during hydrostatic compression of the rock sample (e.g., Fjaer et al., 2021). Microfracture length and aperture can also be measured using micro-CT image data analysis (e.g., Wennberg et al., 2018; Anbari et al., 2019).

Fig. 2a shows calculated capillary pressure curves for partially saturated crack, calculated with equations (11) and (16) for different contact angles, equal to advancing, receding, and to the most stable angle.

It must be noted that the same value of the capillary pressure can correspond to a quite different saturation range due to the hysteresis of the contact angle. At the same time, Fig. 2b shows that the relative permeabilities are uniquely defined versus the saturation degree, calculated for different contact angles, within the range $\theta_r \le \theta \le \theta_a$. This result is relevant only for very thin elliptical cracks with $a \gg b$ because, in thin cracks, the interface curvature has a minor effect on the relative permeability calculation. Next, we will investigate the effect of different waveforms and wave amplitudes on the stimulation of relative permeabilities. Numerical examples are split into two parts: the vibration state on the left side and the relaxation state on the right side of Fig. 3.

After the passage of the elastic wave, the relaxation is taking place on a much longer time scale because the relaxation time is much longer than the vibration period; therefore, we cannot use the same horizontal scale to show both vibration and relaxation. The black curve in Fig. 3a shows the wave-stress versus time for the Ricker waveform with a central frequency of 25 Hz. Blue and red curves show wave-induced fluid pressure changes in the wetting and nonwetting phases versus time in Fig. 3a. It shows that after the passage of the elastic waves, the wave-stress and wave-induced changes in fluid pressure return to their initial state according to equations (20) and (21); therefore, Fig. 3b shows just zero values. The positive values of the wave-stress correspond to tension or decrease in confining stress. Contrary, the positive values of the fluid pressure change in Fig. 3a correspond to increased pressure. Fig. 3c and d shows that an elastic wave induces a residual strain after the passage of elastic wave, although the residual values of stress and pore pressure (in each phase) are zero. At the same time, the residual change in fluid saturation is not equal to zero, as shown below. Therefore, the volume-averaged change in fluid pressure inside the crack is not equal to zero after the passage of the elastic wave. This explains the residual strain value. Furthermore, Fig. 3c shows that the wave amplitude is much larger than typical values during seismic wave propagation (10^{-8}…10^{-6}). Fig. 3e shows that at time = 0.047 s The contact angle reaches its minimum value, equal to the receding angle. This corresponds to a wave-strain $\varepsilon_{REV} = 9.45 \bullet 10^{-6}$ and a wave-stress of 2.2 bars. At this time, the contact line starts to move in the receding direction, causing a reduction of the wetting phase saturation inside the crack, as shown in Fig. 3g. If the wave amplitude is smaller than $\varepsilon_{REV} = 9.45 \bullet 10^{-6}$, the contact line will remain pinned, and thus the saturation inside the crack will not change. Fig. 3i shows the decrease in brine saturation, causing the increase in relative oil permeability and reducing relative brine permeability, as expected according to Fig. 2b. Fig. 3e shows that after the passage of elastic waves, the relative permeabilities relax exponentially to their pre-vibration values due to the relaxation of the contact angle. Fig. 3 shows that all parameters, return to their initial pre-vibration values. These calculations demonstrate that changes in relative permeabilities are triggered by mobilization of the contact line, causing changes in the fluid saturation of the crack. Thus, if the wave amplitude is smaller than $\varepsilon_{REV} = 9.45 \bullet 10^{-6}$, the elastic wave will not change relative permeabilities in this case. Another example can help us understand how relative permeabilities will change with wave

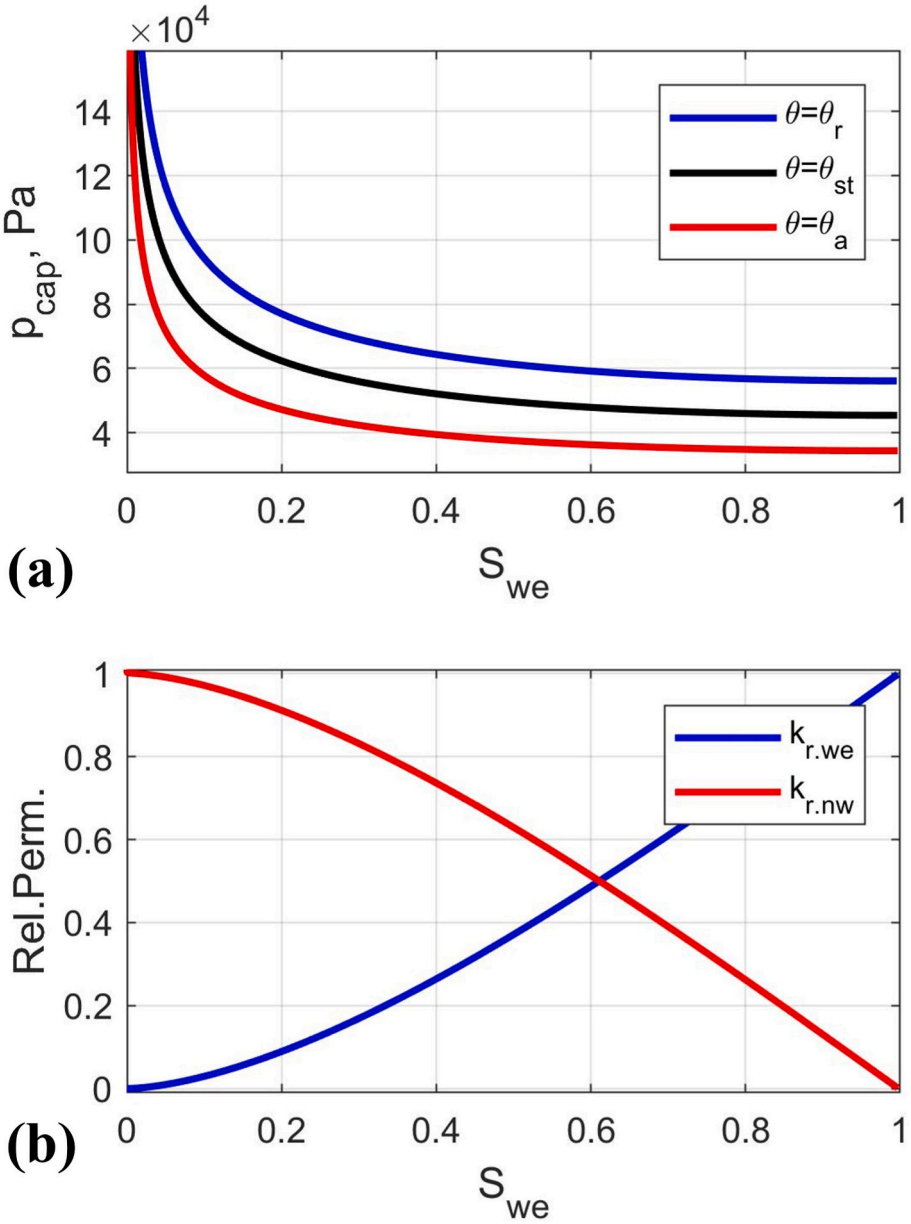

Fig. 2. (a) Capillary pressure vs saturation curves for partially saturated crack, calculated for different contact angles: receding, most stable, and advancing. (b) Relative permeabilities vs saturation curves calculated for partially saturated crack (same curves for different contact angles $\theta_r \leq \theta \leq \theta_a$). Input parameters: Case # 1 in Table 1.

amplitude increase. Fig. 4 shows the case when the wave amplitude is increased approximately two times.

In this example, the contact angle reaches both the advancing angle during the compressional phase and the receding angle during the extensional phase, as shown in Fig. 4e. During the compressional phase, the contact line moves in an advancing direction, and the brine saturation decreases inside the crack. During the extensional phase, the contact line moves into a receding direction, and the brine saturation increases inside the crack, as shown in Fig. 4g. This will decrease the relative oil permeability during the compressive phase and increase relative oil permeability during the extensional phase, as shown in Fig. 4i. Contrary, the relative brine permeability is increasing during the compressive phase and decreases during the extensional phase. Overall, the residual (stimulated) value of relative oil permeability has decreased below the initial value, as shown in Fig. 4i, and increase above the initial value, as shown in Fig. 3i. Therefore, the increase of the wave amplitude for the Ricker wavelet did not cause the expected improvement in relative oil permeability.

Next, we will apply only extensional pulses (positive sinus), as shown in Fig. 5. In this case, the contact angle will reach only the receding value, and the contact line will slip only in the receding direction, causing the reduction of water saturation inside the crack, as shown in Fig. 5e and g.

As a result, the oil phase relative permeability will increase. Let us now increase the wave amplitude by factor 2, as shown in Fig. 6.

Contrary to the Ricker wavelet, the increase in amplitude for extensional pulses is causing a further enhancement of the relative oil permeability, as shown in Fig. 6i. Again, all relative permeabilities and other parameters relax to their pre-vibration stage after the passage of elastic wave, as shown on the right-hand side of Fig. 6.

Let us now consider another relevant example: compressional pulses (negative sinus), as shown in Fig. 7. It is extremely interesting to note that despite identical wave-stress amplitudes and frequencies, waves with different polarities have the opposite effect on the change of

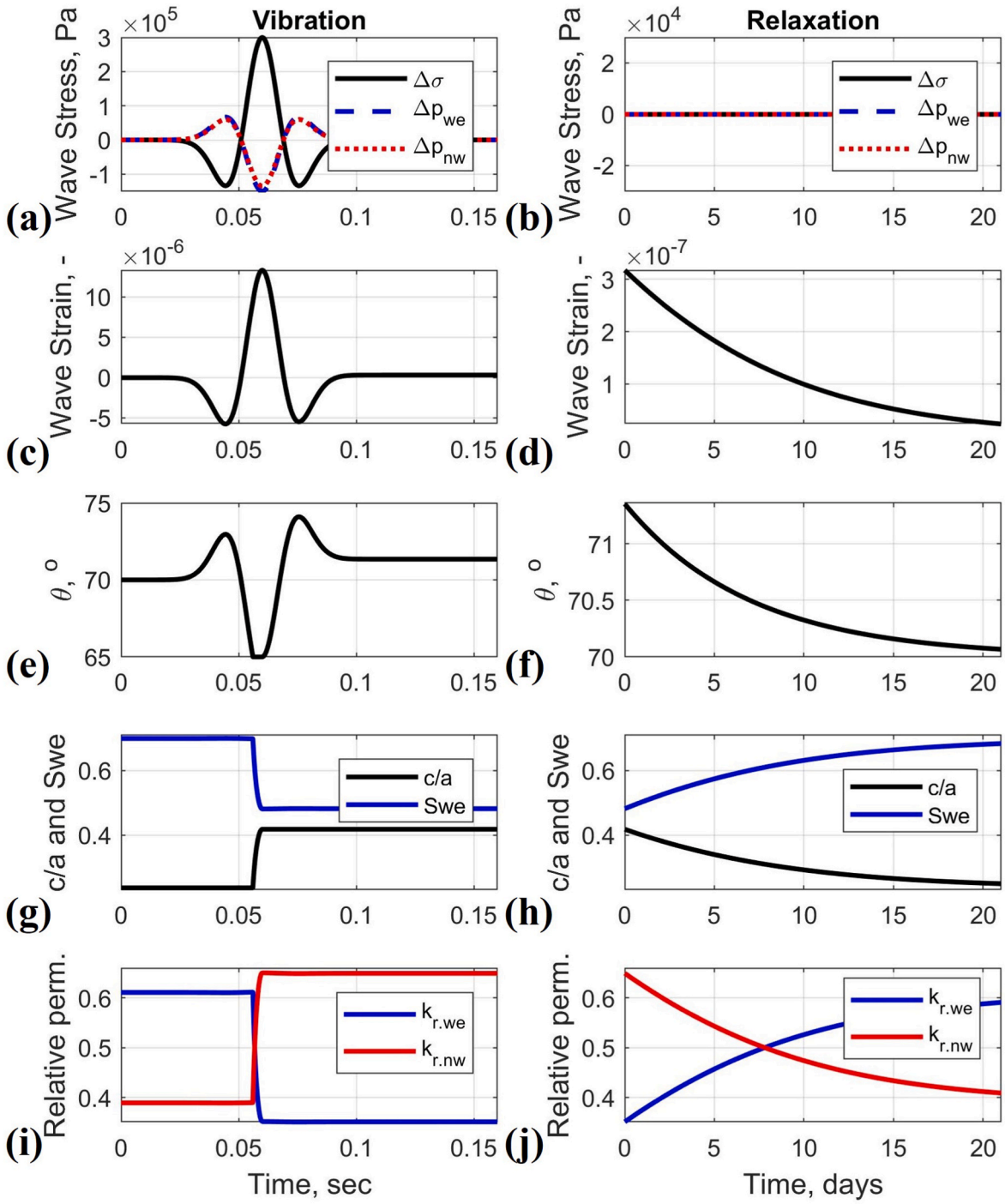

Fig. 3. (a & b) vibration and relaxation of wave-stress and wave-induced pressure changes in the wetting and nonwetting phases vs. time. (c & d) vibration and relaxation of wave-strain vs. time. (e & f) vibration and relaxation of contact angle vs. time. (g & h) vibration and relaxation of brine saturation and contact line location vs. time. (i & j) vibration and relaxation of relative permeabilities vs. time. Input parameters: Case # 1 in Table 1.

relative permeability compare Figs. 5 and 7. The relative oil-phase permeability increases during extensional pulsing (Fig. 5i) and decreases during compressional pulsing (Fig. 7i). Let us now consider another example in Fig. 8: sinusoidal excitation. The amplitude of sinusoidal excitation is the same as the amplitude of extensional and compressional pulses in Figs. 5 and 7. We analyse both the residual changes of relative permeabilities and time-averaged changes of relative permeabilities during sinusoidal vibration. The residual value after the finishing of sinusoidal oscillation depends on the phase of the last vibrational semi-period. Calculation shows that the residual value, shown in Fig. 8j, is the same as the residual value shown in Fig. 5j, because the phase of the last semi-period of sinusoidal vibration is extensional. If the phase of the last semi-period is compressional, the residual value will coincide with Fig. 7j. Next, we will compare time-averaged values during elastic vibrations. Fig. 8i shows that the time-averaged values of relative permeability change are significantly lower than their peak values; contrary, time-averaged values in Figs. 5i and 7i nearly coincide with their peak values. It means that pulse-like vibrations are significantly more efficient than sinusoidal-like vibrations. This has been observed experimentally by Cherskiy et al. (1977), who

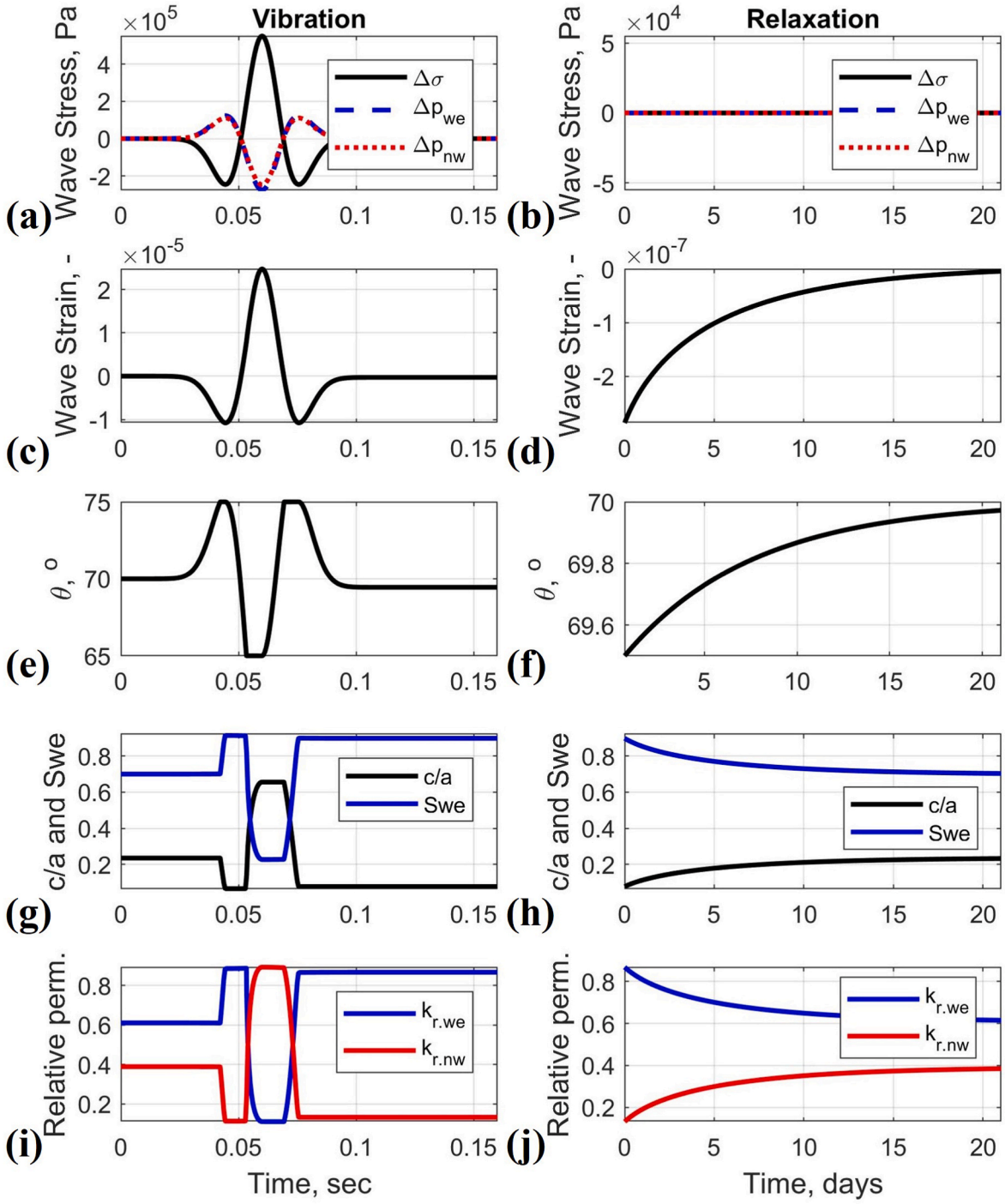

Fig. 4. (a & b) vibration and relaxation of wave-stress and wave-induced pressure changes in the wetting and nonwetting phases vs. time. (c & d) vibration and relaxation of wave-strain vs. time. (e & f) vibration and relaxation of contact angle vs. time. (g & h) vibration and relaxation of brine saturation and contact line location vs. time. (i & j) vibration and relaxation of relative permeabilities vs. time. Input parameters: Case # 1 in Table 1. The wave strain amplitude in Fig. 4 is approximately two times larger than in Fig. 3.

demonstrated that excitation in pulse mode is more efficient than excitation in continuous (sinusoidal) mode (see also Beresnev and Johnson, 1994). Although experiments were conducted at ultrasonic frequencies and details about the saturation control or the shape of elastic pulses were not reported by Cherskiy et al. (1977). The above calculations also show that during pulse-like vibrations, it is possible to achieve both positive and negative effects on time-averaged changes in relative oil permeability (Figs. 5i and 7i). In contrast, during sinusoidal vibrations, the time-averaged change of relative oil permeability is negative (Fig. 8i). All calculation examples presented above correspond to input parameters for Case 1 in Table 1.

These results show that calculated wave amplitudes are much larger than typical strain values during seismic wave propagation ($10^{-8}…10^{-6}$). Next, we will investigate the impact of different input parameters, given for Case 2 in Table 1. Fig. 9 shows calculation results for Case 2 in Table 1. Similar to Figs. 5 and 6, the relative oil permeability has increased during extensional wave-stress pulses; however, the wave-strain amplitude required for its change is much smaller

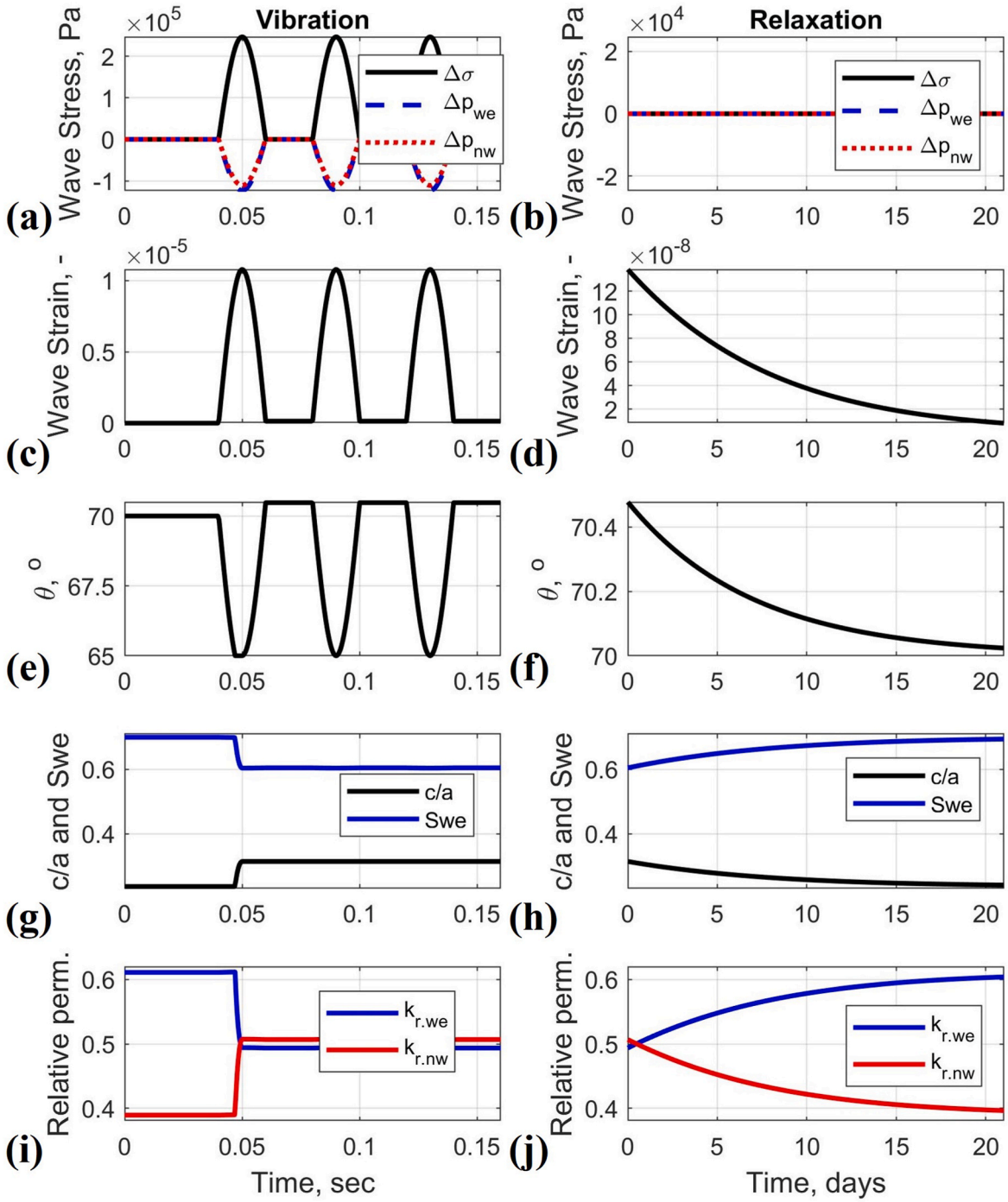

Fig. 5. (a & b) vibration and relaxation of wave-stress and wave-induced pressure changes in the wetting and nonwetting phases vs. time. (c & d) vibration and relaxation of wave-strain vs. time. (e & f) vibration and relaxation of contact angle vs. time. (g & h) vibration and relaxation of brine saturation and contact line location vs. time. (i & j) vibration and relaxation of relative permeabilities vs. time. Input parameters: Case # 1 in Table 1. The wave strain amplitude in Fig. 5 is approximately equal to the case in Fig. 3, but the shape of the waveform is different: extensional pulses in Fig. 5 vs. Ricker waveform in Fig. 3.

$\sim 2 \bullet 10^{-7}$.

This wave amplitude is typical for seismic wave propagation. Finally, we will investigate the effect of different initial water saturation of the crack. In all examples above, shown in Figs. 3–9, we presented results for the initial water saturation of the crack equal to 70% ($S_{we} = 0.7$). In Fig. 10, we present results for the initial water saturation of the crack equal to 30% ($S_{we} = 0.3$) and calculated for Case 2 in Table 1.

Fig. 10 shows that a much larger wave amplitude ($\sim 10^{-6}$) is required for stimulating the oil relative permeability for the case when the initial water saturation is 30%, compared to 70% of water saturation, as shown in Fig. 9.

3. Preliminary laboratory experiments

Our theoretical model described in the previous section demonstrates the possibility of relative permeabilities alteration in the dual-porosity dual-permeability rock by applying small-strain seismic excitations. Notably, the model demonstrates that alteration of relative permeabilities depends both on the amplitude-spectrum and phase-spectrum (or polarity) of the seismic waveform. The dependence of

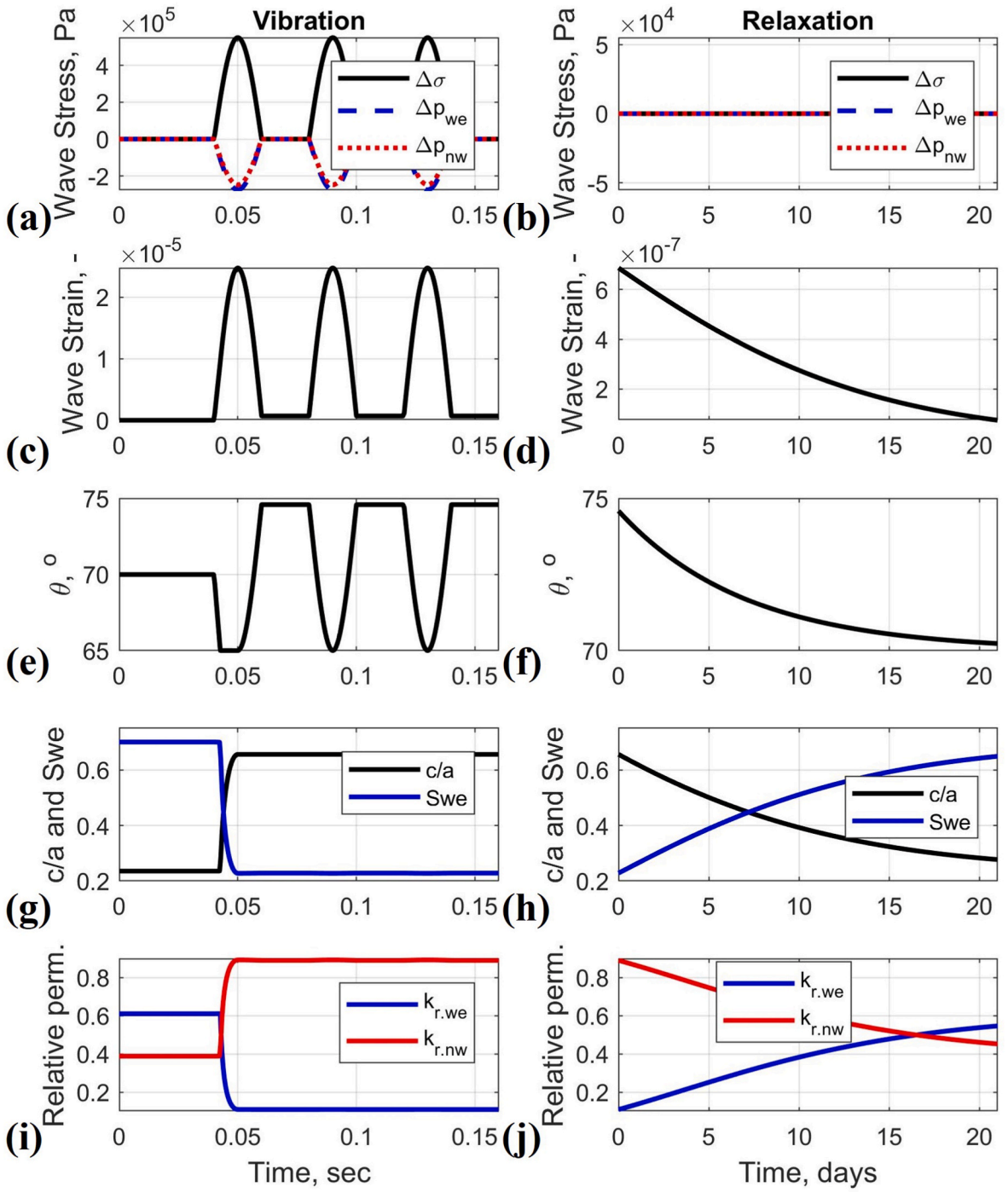

Fig. 6. (a & b) vibration and relaxation of wave-stress and wave-induced pressure changes in the wetting and nonwetting phases vs. time. (c & d) vibration and relaxation of wave-strain vs. time. (e & f) vibration and relaxation of contact angle vs. time. (g & h) vibration and relaxation of brine saturation and contact line location vs. time. (i & j) vibration and relaxation of relative permeabilities vs. time. Input parameters: Case # 1 in Table 1. The wave strain amplitude in Fig. 6 is approximately two times larger than in Fig. 5.

multiphase fluid flow on seismic amplitudes and frequencies have been actively discussed in previous publications (Shmonov et al., 1999; Beresnev and Johnson, 1994; Roberts et al., 2003; Pride et al., 2008; Manga et al., 2012; Nikolaevskiy et al., 1996; Kouznetsov et al., 1998). However, to the best of our knowledge, no publication describes the effect of waveform polarity on multiphase fluid flow. Therefore, the objectives of the laboratory study presented below are to demonstrate that a multiphase fluid flow in dual-porosity dual-permeability rocks can be affected by low-frequency (<200 Hz) small-strain ($\sim 10^{-6}$) seismic waves, and this effect depends on the waveform's polarity.

To validate theoretical results in the lab, we developed a unique low-frequency experimental setup, shown in Fig. 11 (Lozovyi, 2018). The equipment consists of:

- Low-frequency pressure cell mounted into triaxial loading frame
- Custom-built 2-inch diameter endpieces for sample flooding
- Pore fluid system with a low dead volume (2 ml) and the following components:
  - o Differential pressure sensor (between sample inlet and outlet)
  - o Absolute pore pressure sensor (at outlet side)

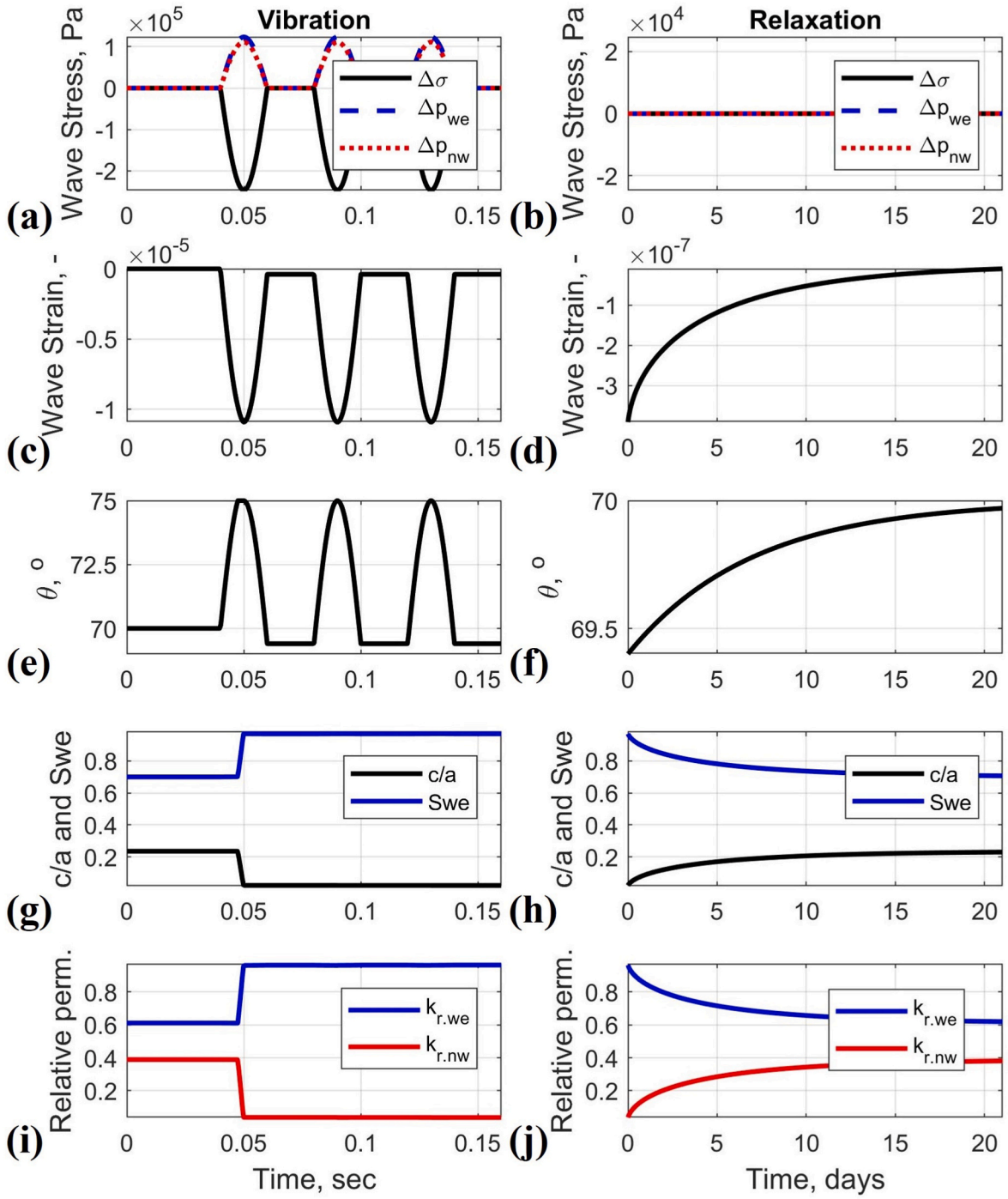

Fig. 7. (a & b) vibration and relaxation of wave-stress and wave-induced pressure changes in the wetting and nonwetting phases vs. time. (c & d) vibration and relaxation of wave-strain vs. time. (e & f) vibration and relaxation of contact angle vs. time. (g & h) vibration and relaxation of brine saturation and contact line location vs. time. (i & j) vibration and relaxation of relative permeabilities vs. time. Input parameters: Case # 1 in Table 1. Fig. 7 needs to be compared with Fig. 5: the same wave strain amplitudes and shapes but different polarities (compressional pulses in Fig. 7 vs. extensional pulses in Fig. 5).

- Back-pressure valve
- Programmable auto-sampler for collecting produced fluids
- Fluid pumps (for brine and oil)

- Pulse generating system with
  - A custom-built hydraulic cylinder for confining pressure oscillations
  - A piezoelectric element inside the cell for axial stress oscillations
  - A pulse-generating workstation with in-house developed software
  - An amplifier
- Data acquisition workstation

The laboratory equipment allows the application of seismic vibrations of a specific frequency, waveform, and polarity during drainage or imbibition flooding cycles of core sample. Fig. 12a shows an example of applied confining stress pulses of different shapes, frequencies, and amplitudes. It also shows measurements of corresponding changes in pore pressure. Produced oil and water are continuously sampled during flooding experiments with vibrations, as shown in Fig. 12b and c.

Experiments were conducted on a 2-inch diameter cylindrical sample of Bentheimer sandstone sample with 22.8% Helium porosity. After drilling and grinding, the Bentheimer sample was mounted into the low-

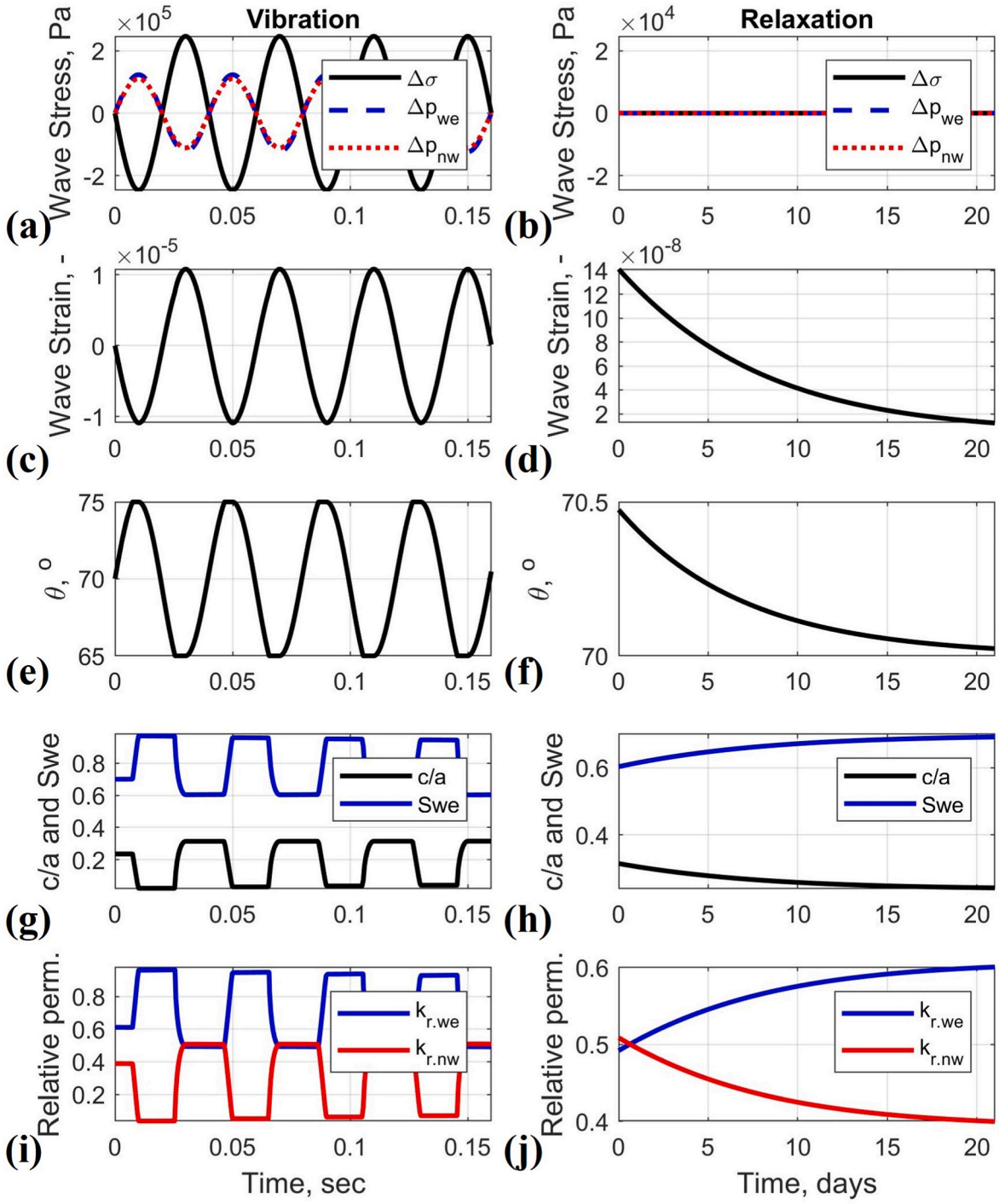

Fig. 8. (a & b) vibration and relaxation of wave-stress and wave-induced pressure changes in the wetting and nonwetting phases vs. time. (c & d) vibration and relaxation of wave-strain vs. time. (e & f) vibration and relaxation of contact angle vs. time. (g & h) vibration and relaxation of brine saturation and contact line location vs. time. (i & j) vibration and relaxation of relative permeabilities vs. time. Input parameters: Case # 1 in Table 1. Fig. 8 needs to be compared with Figs. 5 and 7: Fig. 8 shows the sinusoidal wave, while Figs. 5 and 7 show positive and negative sinus, respectively.

frequency cell for permeability measurements at different effective confining stresses (hydrostatic) ranging from 0.5 to 15 MPa. The results show a permeability of about 1.9 Darcy for the whole range of applied effective confining stresses. The absence of stress dependence indicates that the rock does not contain stress-sensitive cracks. Since the theoretical model predicts the strongest effect in rocks containing microfractures, it was decided to artificially increase the crack porosity of the Bentheimer sandstone. To this end, a fully water saturated sample was treated with liquid nitrogen. Freezing is supposed to thermally expand the pore water and induces cracks in the rock grain frame. Six freezing-thaw cycles were performed. Before and after each cycle compressional ultrasonic velocities in axial and radial directions were measured to assess the evolution of microfractures. After the freezing cycles, permeability measurements were repeated at the same stress levels as before. The results show stress sensitivity of the permeability with a maximum value of 2.3 Darcy at 0.5 MPa effective confining stress. The permeability gradually decreases to 1.9 Darcy at 5 MPa effective confining stress and stays unchanged in the stress range up to 15 MPa

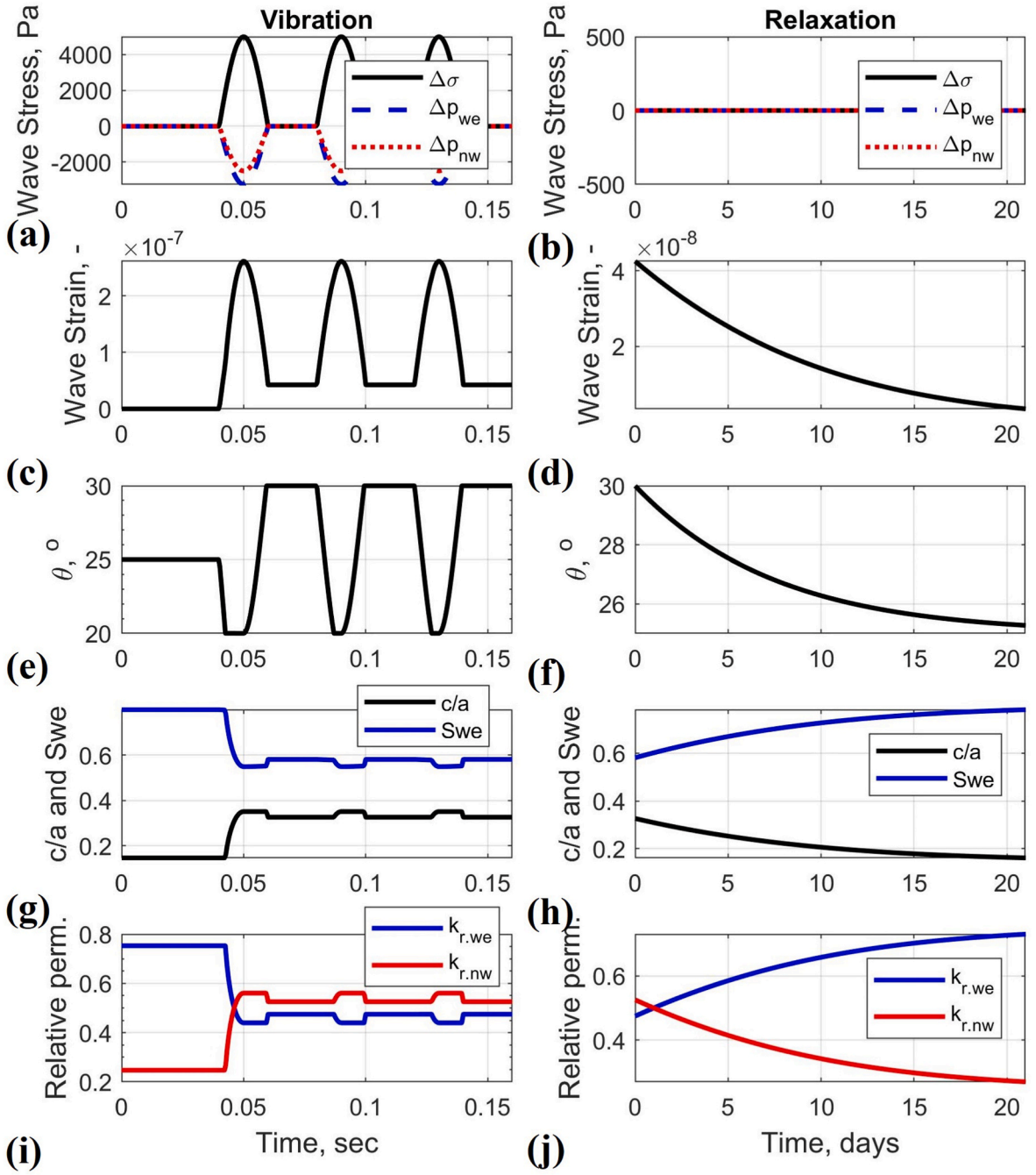

Fig. 9. (a & b) vibration and relaxation of wave-stress and wave-induced pressure changes in the wetting and nonwetting phases vs. time. (c & d) vibration and relaxation of wave-strain vs. time. (e & f) vibration and relaxation of contact angle vs. time. (g & h) vibration and relaxation of brine saturation and contact line location vs. time. (i & j) vibration and relaxation of relative permeabilities vs. time. Input parameters: Case # 2 in Table 1. Fig. 9 needs to be compared with Figs. 5 and 6: much smaller wave amplitude is required for changing relative permeabilities when different input parameters are used.

(see Fig. 5 in Supporting Materials). An excess microfracture permeability of 0.4 Darcy at 0.5 MPa effective confining stress is likely to have been induced by the freezing-thawing cycles. The measurements indicate that the total permeability is not dominated but only slightly (marginally) affected by microfractures (17% of total permeability at 0.5 MPa). Microfracture porosity at the zero effective confining stress was estimated using two different methods. An approach based on weight change of the saturated rock sample, suggests/yields a microfracture porosity of 0.7%. The second method, using more difficult to detect sample volume changes, gives 0.2%. The discrepancy between these two values could be related to the experimental error. These data show that fluid storage occurs predominantly in the matrix, while the fluid flow is slightly affected by the presence of microfractures at low effective confining stresses.

Thus, according to our model, applying small stress vibrations to partially saturated rocks will induce two-phase fluid flow between fracture and matrix. Changes in matrix saturation will be negligibly small because most of the fluid is stored in a matrix. In contrast, changes in microfracture saturation may not be small. Those changes will affect the relative permeabilities of the microfractures, however they will not affect the relative permeabilities of the matrix because relative permeabilities depend on saturation (e.g., Brooks and Corey, 1966). Overall, the impact on relative permeabilities of the sample would be proportional to the change of relative permeabilities of microfracture

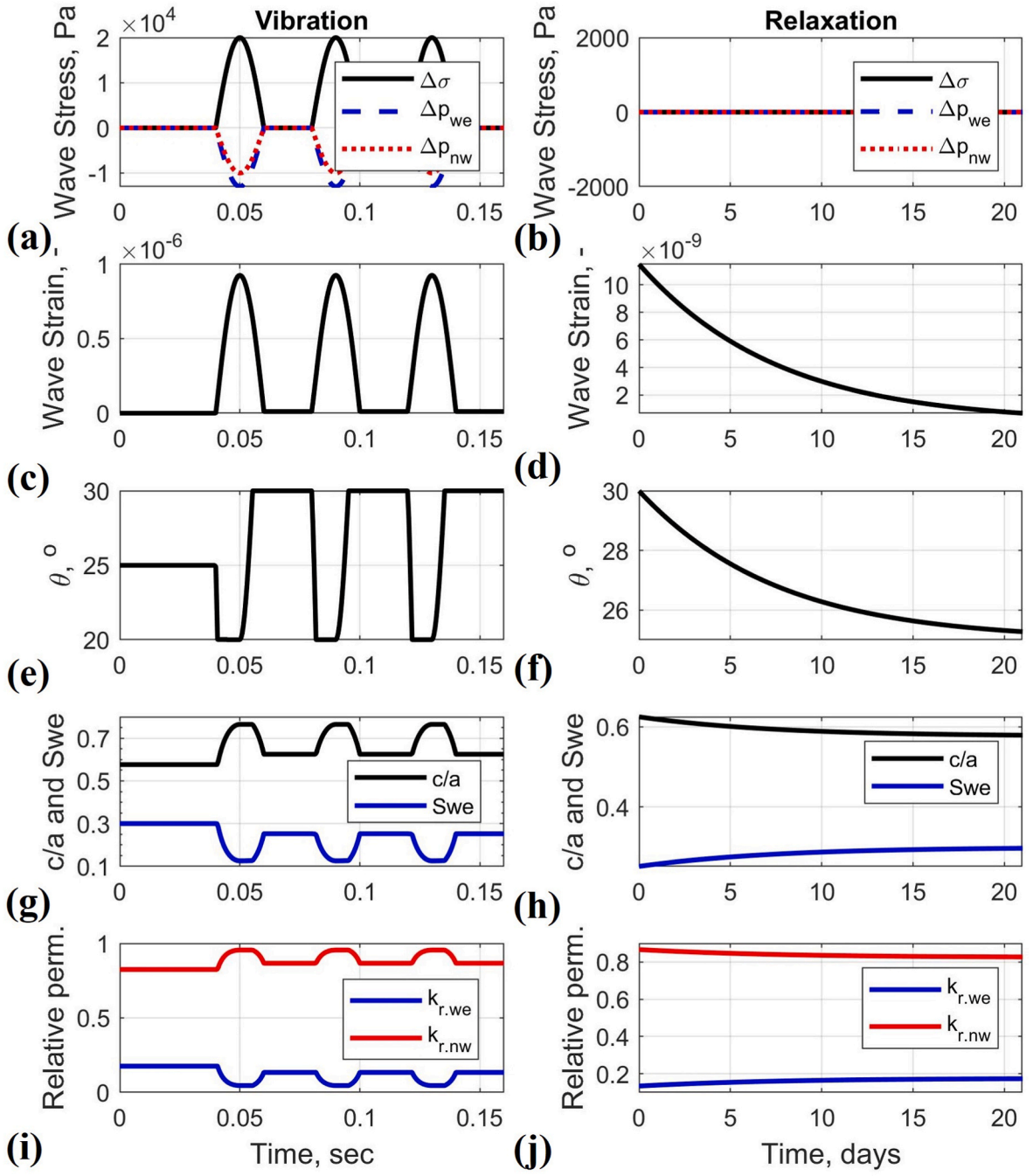

Fig. 10. (a & b) vibration and relaxation of wave-stress and wave-induced pressure changes in the wetting and nonwetting phases vs. time. (c & d) vibration and relaxation of wave-strain vs. time. (e & f) vibration and relaxation of contact angle vs. time. (g & h) vibration and relaxation of brine saturation and contact line location vs. time. (i & j) vibration and relaxation of relative permeabilities vs. time. Input parameters: Case # 2 in Table 1. Compare: In Figs. 3–9, we presented results for initial water saturation of the crack = 70%, while in Fig. 10 it is 30%.

multiplied by the factor 0.17, because the microfracture permeability is 17% of total permeability in these experiments. Therefore, on this particular sample, one would not expect any significant effect of small stress vibrations on changes of relative permeabilities. It must be noted that the relative permeability is not an additive and intrinsic property like porosity, because it depends on the fracture orientation, flow direction, flow rates (fluid viscosity), wettability, interfacial tension, pore connectivity, etc. Therefore, the calculations presented above can be used as an approximation of what can be expected in flooding experiments with seismic excitations.

Another aspect in these experiments is related to the wettability of the core sample. Outcrop samples, as used in our experiment, are generally strongly water wet. In contrast, reservoir rocks exposed to hydrocarbon on the geological timescale are typically weakly water-wet or mixed-wet (Abdallah et al., 1986). It means that the spontaneous imbibition during water flooding of an oil-saturated outcrop sample can significantly affect experimental results. Here, spontaneous imbibition is the process by which a wetting fluid is drawn into a porous medium by capillary action (Morrow and Mason, 2001). This process only occurs when the wetting fluid displaces the non-wetting fluid out of the pore-space. Thus, oil can be recovered in water-wet systems by spontaneous imbibition, replacing the oil originally in the matrix pores with water. Spontaneous imbibition does not take place in oil-wet systems, because oil is captured in the matrix by negative capillary forces.

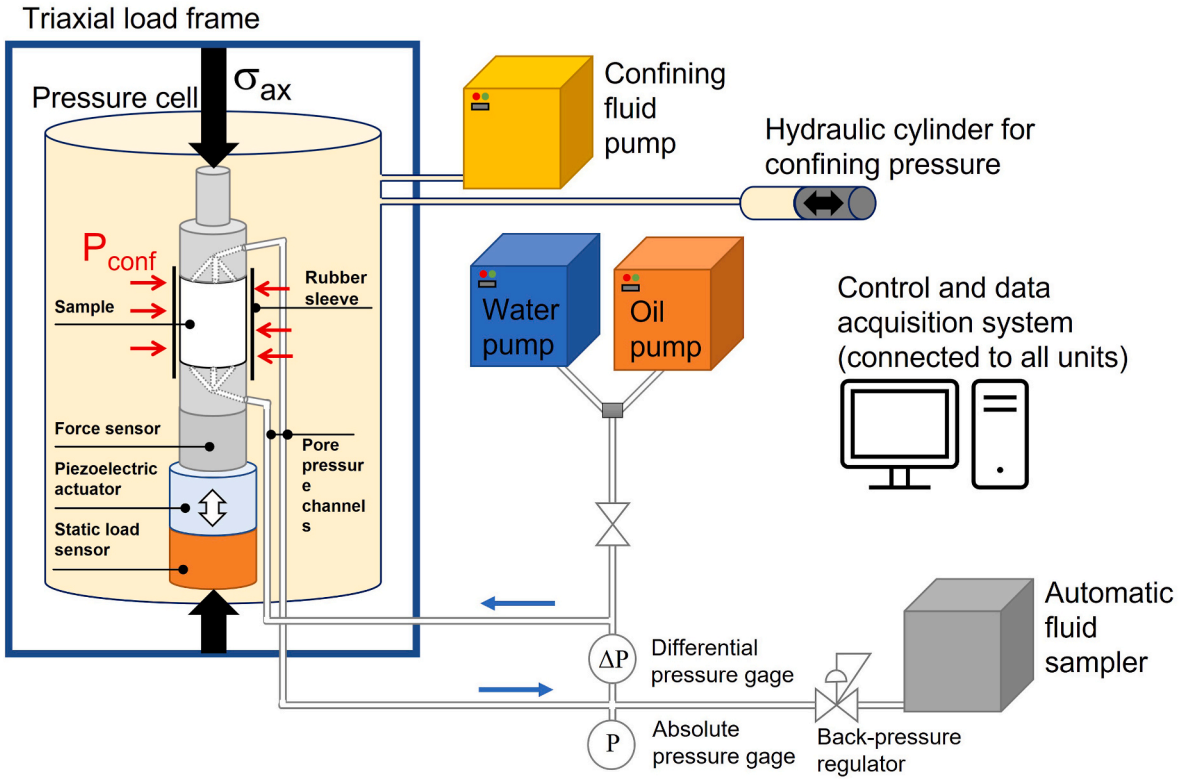

Fig. 11. Experimental setup (see supporting materials for more details).

Therefore, spontaneous imbibition can dominate the response in strongly water-wet systems such as outcrop samples. At the same time, spontaneous imbibition may not be that significant at the reservoir conditions because the rock is much less adhesive to water. In flooding experiments, it is challenging to separate different recovery mechanisms, such as spontaneous imbibition and the effect of seismic excitations. The theoretical model developed in the paper addresses only the effect of seismic excitations; therefore, we focused only on this mechanism in our experiments. Water-saturated samples were flooded with oil and the effect of seismic excitations on water production was assessed. In our case of a water-wet water-saturated sample, spontaneous imbibition will not affect the results during oil flooding.

3.1. *Flooding experiments*

Experiments are conducted at the confining pressure $P_c = 3$ MPa and pore pressure $P_f = 2.5$ MPa on an initially 100% brine saturated sample with a NaCl concentration of 35 ppt. The following successive testing stages were performed on the fractured Bentheimer sandstone sample:

- Drainage-1. The sample is flooded with lamp oil (viscosity - 1.31 cp, density – 0.742 s.g.) at several flow rate stages. Irreducible brine saturation at the final stage (with maximum flow rate 20 ml/min) is $S_{wi} = 18\%$.
- Imbibition-1. The sample is flooded with brine at low rates. It was the intended target stage for pulse testing; however, due to the strong water-wet nature of the sample, spontaneous imbibition occurred at a low flow rate, leaving no possibilities of further oil production. Residual oil saturation $S_{or} = 38\%$.
- Drainage-2. Seismic pulses were applied during this drainage stage to demonstrate the possibility of increasing water production instead of oil since the physical mechanism of stimulating production is the same. Confining pressure pulses were applied during flooding at a 0.1 ml/min rate, axial stress pulses were applied at 0.5 ml/min rate and demonstrated additional brine production.

Table 2 summarizes the results for the Drainage-2 phase; it provides information on injected oil volume, injection rate, produced volumes of each phase, saturation, type of applied pulses.

Note that strain amplitude is not measured directly; it is estimated based on the assumption that the sample's Young's modulus is 5 GPa. Sample stiffness was estimated from ultrasonic velocities and low-frequency stiffness measurement on a similar sample. Estimates of the produced brine volume during pulsed stages of the test are based on optical measurement of the bubbles size (Fig. 12c) and therefore have large uncertainty.

Prior to Drainage-2, during the imbibition stage, the sample was flooded with brine at a maximum differential pressure of 2.5 bar, and irreducible oil saturation of $S_{or} = 38\%$ was achieved. The Drainage-2 stage of the experiment started with oil flooding from the top of the sample with an injection rate of 0.1 ml/min. The differential pressure was stabilized after oil breakthrough. 11.8 ml of brine was produced during this stage, which left the sample with 34.7% brine saturation (see Table 2). After brine expulsion had ceased, 6 different types of confining pressure pulses were applied. The average frequency content for all confining pressure pulses is 1 Hz due to the technical limitations of the system. An example of confining, pore, and differential pressure response on applied pulses is shown in Fig. 12. No brine was produced as a result of confining pressure pulses. Volumes of injected oil, duration of application of each pulse type, and mean frequency are provided in Table 2.

Since confining pressure pulses did not induce any extra production, it was decided to increase the rate to check whether the brine was available for production. Flow rate increase from 0.1 to 0.5 ml/min led to reduction of brine saturation from 34.7% to 28.5% (see Table 2). More than 50 sample pore volumes were injected at a 0.5 ml/min flow rate to make sure equilibrium was reached, and water production was finished. Thereafter, axial stress oscillations were applied that led to the expulsion of brine bubbles (Table 2).

Fig. 12b and c shows vials filled with produced oil and expelled tiny brine bubbles. Examples of stress, strain, and differential pressure

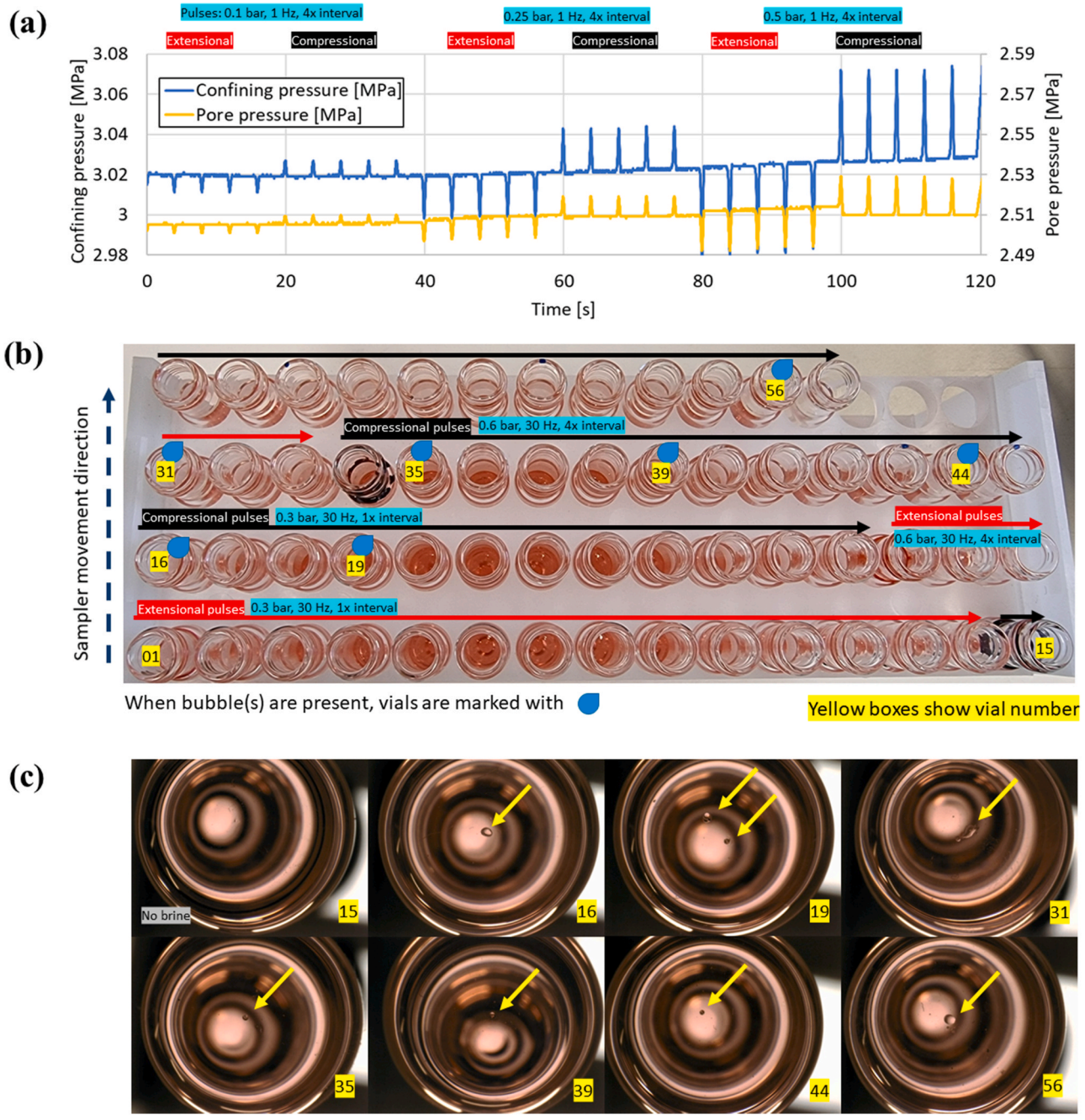

Fig. 12. (a) Example of confining pressure pulses that were applied to the sample according to Table 2. (b) Photograph of sampled oil and water during stages with differential stress pulses at 30 Hz. (c) Photographs of selected vials with water bubbles inside (highlighted by arrows) produced during stages with differential stress pulses at 30 Hz.

response on axial pulses of each applied type during Drainage-2 are provided in Supporting Materials. For stages 1a and 1 b, brine production was only observed after the application of compressional pulses, which agrees with a theoretical model. For stages 1c and 1 d, brine production was occasionally observed during the application of extensional pulses; however, most brine bubbles are produced during compressional pulses. No brine was produced during stage 1e. At the end of Drainage-2, the flow rate was increased to 20 ml/min, which led to achieving irreducible brine saturation of $S_{wi} = 15\%$. This is consistent with Drainage-1 ($S_{wi} = 18\%$).

The volume of produced brine bubbles varied around 0.1 μl. We estimate the amount of brine produced during the application of different pulse types between 1 and 3 μl. This results in an increase of brine production by 0.04%–0.11% at a given constant flow rate of 0.5 ml/min.

3.2. Summary of lab experiments

A unique experimental setup and experimental methods were developed to verify the possibility of increasing hydrocarbon production by applying small-strain seismic excitations to sandstones with microcrack porosity as predicted by a theoretical model. Experimental results obtained during unsteady-state oil flooding of water-saturated Bentheimer sandstone with artificially induced microcrack porosity

demonstrate that the application of seismic pulses increases water production. It is observed that confining pressure pulses with a mean frequency of 1 Hz and amplitude up to 0.5 bar do not affect the production. However, differential stress pulses with a mean frequency of 30 Hz and strain amplitude on the order of μstrain result in additional water production. Thus, depending on rock and fluid properties, only the proper direction of pulses is responsible for additional fluid production as predicted by theory. Considerable efforts were made to develop and improve testing systems, find optimal testing materials, and establish testing methodology and procedures. Finally, a successful demonstration of the studied physical mechanism was achieved in a final experimental attempt, which is only a first step in studying the hydrocarbon recovery stimulation by seismic pulses. Our main finding is that experimental observations are consistent with the theoretical concept, and stimulation of rock by seismic pulses can lead to increased recovery. Further studies are recommended for a better understanding of stimulating mechanisms and possible practical application in reservoir conditions.

3.3. Lessons learned

It is recommended to run laboratory tests on rock samples where fluid flow occurs primarily in the microfracture network while the fluid storage occurs primarily in the matrix. Published laboratory data shows examples of such ideal sandstone candidates, as shown in Table 3. Data for Adamswiller, Berea, Boise, and Darley Dale sandstones in Table 3 are taken from Zhu and Wong (1997), while the Bentheimer data is from this study on a microfractured sample. The data for Adamswiller, Berea, and Darley Dale shows a very high sensitivity of permeability on the effective confining stress. However, the porosity sensitivity on the effective confining stress is very weak. These data indicate that the fluid flow occurs primarily in soft pores, while the fluid storage occurs in stiff pores. At the same time, the data for Boise and Bentheimer sandstones shows a very low sensitivity of permeability on the effective confining stress.

These data for Boise and Bentheimer show that stiff pores dominate both fluid storage and fluid flow. Absolute permeability values for Bentheimer and Boise sandstone samples are about one order of magnitude larger than permeability values for Adamswiller, Berea, and Darley Dale samples. This implies that laboratory tests on less permeable (but more stress-sensitive) samples would take about ten times more time, such that low flow rates resemble reservoir conditions when capillary forces dominate fluid flow. This was unfortunately not feasible in our case due to time constraints, so we decided to run tests on a more permeable but less stress-sensitive sample.

Finally, we would recommend the use of hydrocarbon reservoir rocks to avoid the masking/unwanted effect of spontaneous imbibition.

4. Discussions

In this work we demonstrate theoretically and supported by preliminary laboratory experiments that: 1) seismic waves could affect two-phase fluid flow; 2) this effect can be either positive or negative; 3) the effect depends on the waveform amplitude and polarity 4) fluid mobility within a reservoir recovers to pre-stimulation value after the excitation is stopped. These effects are caused by redistribution of fluid saturation between stiff pores (matrix) and soft pores (cracks or fractures) due to the contact angle hysteresis phenomenon during wave-induced two-phase fluid flow between stiff and soft pores. Thus, these effects are possible only in rocks where the fluid flow occurs primarily through the fracture network, while fluid storage occurs predominantly in the porous matrix. Dynamic stress amplitudes during seismic wave propagation are usually too small to induce changes of the total permeability; only the relative permeability can be affected. Furthermore, the energy of the low-frequency seismic wave is too small to cause any heating of the formation. Therefore, the method of stimulating hydrocarbon production by seismic excitations can be envisioned to be a complement to standard EOR/IOR methods such as water and gas injection, used for pressure support and oil displacement towards producing wells; hydraulic fracturing, used to enhance total permeability at the reservoir scale; steam injection, used for heavy crude oil viscosity reduction. Changes in relative permeabilities cannot compensate for the total permeability and oil viscosity, affecting the production. The average oil recovery rate for oil fields on the Norwegian shelf is about 47%. However, by improving relative permeabilities with seismic excitations, the oil recovery factor can be increased further.

This paper describes a new model that explains how different waveforms can change the relative permeability of a partially saturated crack. According to the model, extensional pulses are the most efficient to increase the hydrocarbon mobility of a partially saturated crack in the water-wet rocks. The model also predicts a critical wave amplitude required for changes of crack's relative permeabilities. A more detailed discussion about seismic or other sources used to generate those extensional wave pulses of required amplitude at the reservoir depth is outside of the scope of this paper. Moreover, wave propagation from seismic sources to the depth of interest is not dealt with. However, the model can still predict the change of relative permeability if the shape and amplitude of the seismic waveform at the reservoir depth are known.

Nevertheless, we can still discuss the effects of P- and S-waves. Our model investigated the effect of volumetric strain (such as induced by P-wave) on redistribution of fluid saturation between cracks and matrix during wave-induced two-phase fluid flow between crack and matrix. Volumetric strains are independent of the P-wave propagation direction in an isotropic medium. According to our model, S-waves do not produce volumetric deformations in isotropic rock; therefore, fluid pressure changes in each fluid phase are negligibly small. Thus, our model will not predict any changes in fluid saturation and relative permeability of the crack due to S-waves. Hence, our results are opposite to previous studies, for example, Barbosa et al. (2019), who suggested that alteration of fluid mobility is more efficient by S-waves, because S-waves produce viscous shearing approximately two times larger than P-waves. This discrepancy between our results and Barbosa et al. (2019) is due to different physical mechanisms considered: capillary forces versus viscous forces.

Besides, Barbosa et al. (2019) argued that fracture unclogging due to

Table 3
Porosity and permeability of sandstone versus hydrostatic effective confining stress. Modified after Zhu and Wong (1997).

Effective stress, MPa	Adamswiller		Berea		Boise		Darley Dale		Bentheimer	
	Por., %	Perm., x10^{-15} m^2	Por., %	Perm., x10^{-15} m^2	Por., %	Perm., x10^{-15} m^2	Por., %	Perm., x10^{-15} m^2	Por., %	Perm., x10^{-15} m^2
0.5									~22	2270
3	23.0	144	21.0	348	35.0	1864	14.0	65		1964
5			20.8	223	34.5	1721	13.8	34		1875
10	22.0	52	20.3	160	33.5	1650	13.5	22		1885
15					32.9	1453	13.3	15		1875
20	21.4	21	19.8	132	32.3	1126	13.1	12		

mobilization of deposited colloids in the fracture network is much more efficient at a higher frequency. This seems to contradict experimental observations showing that long-period waves are more effective at increasing permeability at a given wave amplitude (Manga et al., 2012). Still, Barbosa et al.'s (2019) model could be more relevant for understanding and preventing water inrush and sand gushing accidents caused by the flow behaviour of water-sand mixtures in the fractured rock masses (Zhang et al., 2021). According to our model, the frequency should be low enough to allow fluids to flow between the crack and matrix and equilibrate the wave-induced pressure gradients in the representative elementary volume.

Additionally, we need to mention that several mechanisms can alter fluid mobilities by transient stresses. This paper investigated the alteration of fluid saturation of the crack driven by capillary forces during wave-induced fluid flow between crack and matrix. Those capillary forces are much more efficient at lower frequencies and disappear if a single fluid phase fully saturates the rock. Contrary, viscous forces responsible for mobilization of colloid deposits in fractures and pore throats (also responsible for sweeping oil droplets) are much more efficient at higher frequencies, such as ultrasonic (Mullakaev et al., 2019) and present during a single-phase fluid saturation. Thus, at intermediate frequencies, these two different physical mechanisms can act simultaneously.

Previous studies showed that upon stopping the dynamic stimulation, the mobility of fluids recovers to prestimulated value after a specific time (e.g., Beresnev and Johnson, 1994; Nikolaevskiy et al., 1996; Manga et al., 2012). Previous scholars argued that recovery of fluid mobilities is related to clogging of pore throats (e.g., Manga et al., 2012) or to clogging of fractures (e.g., Barbosa et al., 2019) by colloidal particles. The question is, why should it be unclogged to the same prestimulated value? There are no physical explanations to this question offered in Manga et al. (2012) and Barbosa et al. (2019). In our model, the recovery of oil-phase and water-phase permeabilities to prestimulated values is explained by the recovery of contact angles to the most stable configuration. This configuration corresponds to the minimum of Gibb's energy (Drelich, 2019). We coupled the alteration of the contact angles with the alteration of phase permeabilities of the rock. Thus, the recovery of contact angles causes the recovery of phase permeabilities to the same prestimulated values. Furthermore, previous models do not explain when the fluid mobility will increase and when it will decrease during/after seismic excitations, while our model can explain this effect. Besides, previous studies do not explain how fluid saturation will affect the efficiency of seismic stimulation. In this study, we showed that the efficiency of seismic stimulation increases with the decrease of oil saturation inside the crack.

The focus of this experimental work was to demonstrate that properly applied pulses would lead to a positive effect on fluid production. Meanwhile, our theoretical model and previous publications show that a negative effect can occur under certain circumstances. This could be proven in another dedicated lab study using suitable samples/material as described in Chapter 3.3.

To conclude this discussion, it is interesting to note that Nikolaevskiy et al. (1996) hypothesized that when rock grains in the reservoir are subjected to low-frequency excitations, they generate high-frequency harmonics. The high-frequency waves create a microscopic flow field, which causes the trapped oil to mobilize. However, according to our recent studies (Rozhko, 2020b, 2021), high-frequency harmonics are generated by the relative motion of immiscible fluid phases at the pore scale, i.e., by mobilization of trapped oil. Thus, we have a discrepancy in causal relationships with the Nikolaevskiy et al. hypothesis.

5. Conclusions

This paper developed a new model to predict changes of crack's relative permeabilities caused by the wave-induced two-phase fluid flow between the crack and matrix and by the contact angle hysteresis phenomenon. We demonstrated that alterations in crack's relative permeability depend on the waveform amplitude and polarity as well as material parameters. The presented model is valid within a low-frequency regime as it allows two-phase fluids to flow between the crack and matrix and equilibrate wave-induced fluid pressure gradients in the representative elementary volume between two consecutive wave cycles.

We showed that extensional pulses cause the increase of oil relative permeability in the water-wet rock, while compressional pulses cause the reduction of oil phase relative permeability. Furthermore, we demonstrated that the elastic excitation in the pulse mode could change relative permeabilities much more efficiently than sinusoidal excitations of the same amplitude. The critical wave amplitude required for the change of relative permeability is reached when the contact angle approaches its critical value (advancing or receding angle), leading to mobilization of the interface meniscus between immiscible fluids inside the crack. Mobilization of the interface meniscus causes alteration of fluid saturation inside the crack, thus changing the crack's relative permeabilities. Depending on the choice of material parameters, the critical wave-strain amplitude could be in the range from $\sim 10^{-7}$ to $\sim 10^{-5}$, while typical wave-strain amplitudes during seismic wave propagation are around $\sim 10^{-8}$ to $\sim 10^{-6}$. Thus, the technology of hydrocarbon recovery stimulation by small seismic excitations may not always be applicable for all reservoir rocks because it requires substantial elastic wave energy, which is difficult to deliver to the reservoir depth. Only in specific cases predicted by our model, this technology may work.

The results of the first laboratory experiment on a sandstone sample support the theoretical predictions and demonstrate increased production when seismic excitations of specific waveforms shape, polarity, amplitude, and frequency are applied.

Further multidisciplinary research is required to better understand the observed changes of hydrological response caused by transient stresses, such as those induced by an earthquake or anthropogenic source. As we demonstrated in this paper, these effects cannot be explained without joint consideration of interfacial science, geophysics, and reservoir engineering.

Credit author statement

Dr. Alexander Y. Rozhko: theory, discussions, manuscript writing. **Dr. Serhii Lozovyi**: lab experiments, discussions, manuscript writing. **Dr. Marcel Naumann**: lab experiments, discussions, manuscript writing. **Dr. Fredrik Hansteen**: discussions, manuscript writing. **Dr. Matteo Ravasi**: discussions, manuscript writing.

Declaration of competing interest

The authors declare that they have no known competing financial interests or personal relationships that could have appeared to influence the work reported in this paper.

Acknowledgements

Equinor ASA is acknowledged for approving the publication.

APPENDIX

In this appendix, we present partial derivatives, which appear in equations (23)–(27). To simplify equations, we will introduce the following auxiliary parameters X and Y:

$$X = 1 - 8p_{cl}\frac{\gamma\cos(\theta)}{\pi b}\frac{\left(\beta + \cot(\beta)\ln[\cos(\beta)] - \frac{\pi}{2}\right)}{\left(p_{cl} + \sigma + p_{we}\right)^2 \sin(\beta)}, \tag{A1}$$

and

$$Y = \beta + \cot(\beta)\ln[\cos(\beta)] - \frac{\pi}{2}. \tag{A2}$$

Finally, partial derivatives are calculated as:

$$\frac{\partial p_{cap}}{\partial \beta} = \frac{\pi(p_{cl} + \sigma + p_{we})}{8\sin(\beta)Y\sqrt{X}}\left((X-1)\cos(\beta) - \frac{\left(\sqrt{X}-1\right)^2 \ln[\cos(\beta)]}{\sin(\beta)Y}\right) \tag{A3}$$

$$\frac{\partial p_{cap}}{\partial \sigma} = \frac{\pi}{4Y}\left(1 - \sqrt{X} - \frac{1-X}{\sqrt{X}}\right), \tag{A4}$$

$$\frac{\partial p_{cap}}{\partial p_{we}} = \frac{\partial p_{cap}}{\partial \sigma}, \tag{A5}$$

$$\frac{\partial p_{cap}}{\partial \theta} = \frac{\pi(X-1)(p_{cl} + \sigma + p_{we})}{8Y\sqrt{X}}\tan(\theta). \tag{A6}$$

Appendix A. Supplementary data

Supplementary data to this article can be found online at https://doi.org/10.1016/j.petrol.2022.110393.

References

Abdallah, W., Buckley, J.S., Carnegie, A., Edwards, J., Herold, B., Fordham, E., Graue, A., Habashy, T., Seleznev, N., Signer, C., Hussain, H., 1986. Fundamentals of wettability. Technology 38 (1125–1144), 268.

Al-Shami, T.M., Jufar, S.R., Negash, B.M., Abdullahi, M.B., 2021. Impact of external excitation on flow behavior of trapped oil blob. J. Petrol. Sci. Eng. 196, 108002.

Ali, M., Aftab, A., Arain, Z.U.A., Al-Yaseri, A., Roshan, H., Saeedi, A., et al., 2020. Influence of organic acid concentration on wettability alteration of cap-rock: implications for CO2 trapping/storage. ACS Appl. Mater. Interfaces 12 (35), 39850–39858.

Ali, M., Jha, N.K., Pal, N., Keshavarz, A., Hoteit, H., Sarmadivaleh, M., 2021. Recent advances in carbon dioxide geological storage, experimental procedures, influencing parameters, and future outlook. Earth Sci. Rev. 103895.

Ali, M., Yekeen, N., Pal, N., Keshavarz, A., Iglauer, S., Hoteit, H., 2022. Influence of organic molecules on wetting characteristics of mica/H2/brine systems: implications for hydrogen structural trapping capacities. J. Colloid Interface Sci. 608, 1739–1749.

AlRatrout, A., Raeini, A.Q., Bijeljic, B., Blunt, M.J., 2017. Automatic measurement of contact angle in pore-space images. Adv. Water Resour. 109, 158–169.

Anbari, A., Lowry, E., Piri, M., 2019. Estimation of capillary pressure in unconventional reservoirs using thermodynamic analysis of pore images. J. Geophys. Res. Solid Earth 124 (11), 10893–10915.

Andrew, M., Menke, H., Blunt, M.J., Bijeljic, B., 2015. The imaging of dynamic multiphase fluid flow using synchrotron-based X-ray microtomography at reservoir conditions. Transport Porous Media 110 (1), 1–24.

Barbosa, N.D., Hunziker, J., Lissa, S., Saenger, E.H., Lupi, M., 2019. Fracture unclogging: a numerical study of seismically induced viscous shear stresses in fluid-saturated fractured rocks. J. Geophys. Res. Solid Earth 124, 11705–11727.

Barenblatt, G.I., Entov, V.M., Ryzhik, V.M., 1990. Theory of Fluid Flows through Natural Rocks. Kluwer Academic Publishers.

Beresnev, I.A., 2006. Theory of vibratory mobilization on nonwetting fluids entrapped in pore constrictions. Geophysics 71 (6), N47–N56.

Beresnev, I.A., Johnson, P.A., 1994. Elastic-wave stimulation of oil production: a review of methods and results. Geophysics 59, 1000–1017.

Berryman, J.G., Wang, H.F., 1995. The elastic coefficients of double-porosity models for fluid transport in jointed rock. J. Geophys. Res. Solid Earth 100 (B12), 24611–24627.

Blunt, M.J., 2017. Multiphase Flow in Permeable Media: A Pore-Scale Perspective. Cambridge University Press.

Blunt, M.J., Lin, Q., Akai, T., Bijeljic, B., 2019. A thermodynamically consistent characterization of wettability in porous media using high-resolution imaging. J. Colloid Interface Sci. 552, 59–65.

Boeut, S., 2020. Variation in Permeability of Rocks Due to Transient Disturbances in Axial Stress or Pore Pressure. Doctoral dissertation. Hokkaido University. http://hdl.handle.net/2115/77980. (Accessed 8 February 2022).

Bormashenko, E., 2013. Wetting of real solid surfaces: new glance on well-known problems. Colloid Polym. Sci. 291 (2), 339–342.

Broadhead, M.K., 2010. Oscillating oil drops, resonant frequencies, and low-frequency passive seismology. Geophysics 75 (1), O1–O8.

Brooks, R.H., Corey, A.T., 1966. Properties of porous media affecting fluid flow. J. Irrigat. Drain. Div. 92 (2), 61–88.

Candela, T., Brodsky, E.E., Marone, C., Elsworth, D., 2014. Laboratory evidence for particle mobilization as a mechanism for permeability enhancement via dynamic stressing. Earth Planet Sci. Lett. 392, 279–291.

Cheng, A.H., 2020. A linear constitutive model for unsaturated poroelasticity by micromechanical analysis. Int. J. Numer. Anal. Methods GeoMech. 44 (4), 455–483.

Cherskiy, N.V., Tsarev, V.P., Konovalov, V.M., Kuznetsov, 0. L., 1977. The effect of ultrasound on permeability of rocks to water, Transactions (Doklady) of the USSR Academy of Sciences. Earth Sci.Sec. 232, 201–204.

Drelich, J., 1999. Instability of the three-phase contact region and its effect on contact angle relaxation. J. Adhes. Sci. Technol. 13 (12), 1437–1455.

Drelich, J.W., 2019. Contact angles: from past mistakes to new developments through liquid-solid adhesion measurements. Adv. Colloid Interface Sci. 267, 1–14.

Elkhoury, J.E., Niemeijer, A., Brodsky, E.E., Marone, C., 2011. Laboratory observations of permeability enhancement by fluid pressure oscillation of in situ fractured rock. J. Geophys. Res. Solid Earth 116 (B2).

Fjaer, E., Holt, R.M., Horsrud, P., Raaen, A.M., 2021. Petroleum Related Rock Mechanics. Elsevier.

Frehner, M., Schmalholz, S.M., Podladchikov, Y., 2009. Spectral modification of seismic waves propagating through solids exhibiting a resonance frequency: a 1-D coupled wave propagation–oscillation model. Geophys. J. Int. 176, 589–600. https://doi.org/10.1111/j.1365-246X.2008.04001.x.

Gassmann, F., 1951. Über die Elastizität poröser Medien. Vierteljahresschrift der naturforschenden Gesellschaft Zürich 96, 1–23.

Hilpert, M., 2007. Capillarity-induced resonance of blobs in porous media: analytical solutions, Lattice-Boltzmann modeling, and blob mobilization. J. Colloid Interface Sci. 309, 493–504. https://doi.org/10.1016/j.jcis.2006.11.052.

Holzner, R., Eschle, P., Dangel, S., Frehner, M., Narayanan, C., Lakehal, D., 2009. Hydrocarbon microtremors interpreted as nonlinear oscillations driven by oceanic background waves. Commun. Nonlinear Sci. Numer. Simulat. 14, 160–173. https://doi.org/10.1016/j.cnsns.2007.06.013.

Jeong, C., Kallivokas, L.F., Kucukcoban, S., Deng, W., Fathi, A., 2015. Maximization of wave motion within a hydrocarbon reservoir for wave-based enhanced oil recovery. J. Petrol. Sci. Eng. 129, 205–220.

Khasi, S., Fayazi, A., Kantzas, A., 2021. Effects of acoustic stimulation on fluid flow in porous media. Energy Fuel. 35 (21), 17580–17601.

Khishvand, M., Alizadeh, A.H., Kohshour, I.O., Piri, M., Prasad, R.S., 2017. In situ characterization of wettability alteration and displacement mechanisms governing recovery enhancement due to low-salinity waterflooding. Water Resour. Res. 53 (5), 4427–4443.

Kouznetsov, O.L., Simkin, E.M., Chilingar, G.V., Katz, S.A., 1998. Improved oil recovery by application of vibro-energy to waterflooded sandstones. J. Petrol. Sci. Eng. 19 (3–4), 191–200.
Lee, K.S., Ivanova, N., Starov, V.M., Hilal, N., Dutschk, V., 2008. Kinetics of wetting and spreading by aqueous surfactant solutions. Adv. Colloid Interface Sci. 144 (1–2), 54–65.
Liu, W., Manga, M., 2009. Changes in permeability caused by dynamic stresses in fractured sandstone. Geophys. Res. Lett. 36 (20).
Lozovyi, S., 2018. Seismic Dispersion and the Relation between Static and Dynamic Stiffness of Shales, p. 182. Doctoral theses at NTNU;2018.
Lu, J.F., Hanyga, A., 2005. Linear dynamic model for porous media saturated by two immiscible fluids. Int. J. Solid Struct. 42 (9–10), 2689–2709.
Manga, M., Beresnev, I., Brodsky, E.E., Elkhoury, J.E., Elsworth, D., Ingebritsen, S.E., Mays, D.C., Wang, C.Y., 2012. Changes in permeability caused by transient stresses: field observations, experiments, and mechanisms. Rev. Geophys. 50, RG2004.
Mascini, A., Cnudde, V., Bultreys, T., 2020. Event-based contact angle measurements inside porous media using time-resolved micro-computed tomography. J. Colloid Interface Sci. 572, 354–363.
Masson, Y.J., Pride, S.R., 2011. Seismic attenuation due to patchy saturation. J. Geophys. Res. Solid Earth 116 (B3).
Mat-Shayuti, M.S., Ya, T.M.Y.S.T., Abdullah, M.Z., Khamaruddin, P.N.F.M., Othman, N. H., 2019. Progress in ultrasonic oil-contaminated sand cleaning: a fundamental review. Environ. Sci. Pollut. Control Ser. 26 (26), 26419–26438.
Mavko, G., Mukerji, T., Dvorkin, J., 2020. The Rock Physics Handbook: Tools for Seismic Analysis of Porous Media. Cambridge university press.
Mirzaei-Paiaman, A., Nourani, M., 2012. Positive effect of earthquake waves on well productivity: case study: Iranian carbonate gas condensate reservoir. Sci. Iran. 19 (6), 1601–1607.
Morrow, N.R., Mason, G., 2001. Recovery of oil by spontaneous imbibition. Curr. Opin. Colloid Interface Sci. 6 (4), 321–337.
Mullakaev, M.S., Saltykov, YuA., Saltykov, A.A., Mullakaev, R.M., 2019. Analysis of pilot testing of ultrasonic technology in the Samotlor field wells: Geology. Geophys. Develop. Oil Gas Fields 7, 71–85.
Müller, T.M., Gurevich, B., Lebedev, M., 2010. Seismic wave attenuation and dispersion resulting from wave-induced flow in porous rocks—a review. Geophysics 75 (5), 75A147–75A164.
Nikolaevskiy, V.N., Lopukhov, G.P., Yizhu, L., Economides, M.J., 1996. Residual oil reservoir recovery with seismic vibrations. SPE Prod. Facil. 11 (2), 89–94.
Papageorgiou, G., Amalokwu, K., Chapman, M., 2016. Theoretical derivation of a Brie-like fluid mixing law. Geophys. Prospect. 64, 1048–1053.
Pouya, A., Vu, M.N., Ghabezloo, S., Bendjeddou, Z., 2013. Effective permeability of cracked unsaturated porous materials. Int. J. Solid Struct. 50 (20–21), 3297–3307.
Pride, S.R., Berryman, J.G., Harris, J.M., 2004. Seismic attenuation due to wave-induced flow. J. Geophys. Res. Solid Earth 109 (B1).
Pride, S.R., Flekkøy, E.G., Aursjø, O., 2008. Seismic stimulation for enhanced oil recovery. Geophysics 73 (5), O23–O35.
Roberts, P.M., Abdel-Fattah, A.I., 2009. Seismic stress stimulation mobilizes colloids trapped in a porous rock. Earth Planet Sci. Lett. 284 (3–4), 538–543.
Roberts, P.M., Esipov, I.B., Majer, E.L., 2003. Elastic wave stimulation of oil reservoirs: promising EOR technology? Lead. Edge 22 (5), 448–453.
Rozhko, A.Y., 2016. Two-phase fluid-flow modeling in a dilatant crack-like pathway. J. Petrol. Sci. Eng. 146, 1158–1172.
Rozhko, A.Y., 2019. Bulk moduli and seismic attenuation in partially saturated rocks: hysteresis of liquid bridges effect. Geophys. Prospect. 67 (5), 1404–1430.
Rozhko, A.Y., 2020a. Comments on "Investigation of the resonance of nonwetting droplets in constricted capillary tubes" by (Chao Zeng, Wen Deng, Jing Fan, and Kelly H. Liu, 2020, Geophysics, 85, no. 2, ID1–ID17). Geophysics 85 (6). X1-X2.
Rozhko, A.Y., 2020b. Effective fluid bulk modulus in the partially saturated rock and the amplitude dispersion effects. J. Geophys. Res. Solid Earth 125 (3).
Rozhko, A.Y., 2021. On the spectral changes of seismic wave energy by a partially saturated crack due to the hysteresis of liquid bridges phenomenon. Geophysics 86 (3), MR133–MR147.
Scanziani, A., Singh, K., Blunt, M.J., Guadagnini, A., 2017. Automatic method for estimation of in situ effective contact angle from X-ray micro tomography images of two-phase flow in porous media. J. Colloid Interface Sci. 496, 51–59.
Scanziani, A., Lin, Q., Alhosani, A., Blunt, M.J., Bijeljic, B., 2020. Dynamics of fluid displacement in mixed-wet porous media. Proc. Roy. Soc. A 476 (2240), 20200040.
Shi, Z., Wang, G., Manga, M., Wang, C.Y., 2015. Mechanism of co-seismic water level change following four great earthquakes–insights from co-seismic responses throughout the Chinese mainland. Earth Planet Sci. Lett. 430, 66–74.
Shmonov, V.M., Vitovtova, V.M., Zharikov, A.V., 1999. Experimental study of seismic oscillation effect on rock permeability under high temperature and pressure. Int. J. Rock Mech. Min. Sci. 36 (3), 405–412, 1997.
Skempton, A.W., 1954. The pore-pressure coefficients A and B. Geotechnique 4, 143–147. https://doi.org/10.1680/geot.1954.4.4.143.
Sun, C., McClure, J.E., Mostaghimi, P., Herring, A.L., Berg, S., Armstrong, R.T., 2020a. Probing effective wetting in subsurface systems. Geophys. Res. Lett. 47 (5) (no-no).
Sun, C., McClure, J.E., Mostaghimi, P., Herring, A.L., Shabaninejad, M., Berg, S., Armstrong, R.T., 2020b. Linking continuum-scale state of wetting to pore-scale contact angles in porous media. J. Colloid Interface Sci. 561, 173–180.
Surguchev, M.L., Kuznetsov, O.L., Simkin, E.M., 1975. Gidrodinamicheskoe, Akusticheskoe, Teplovoe Tsiklicheskoe Vozdeistvie Na Neftyanye Plasty (Hydrodynamic, Acoustic, Thermal Cycling Impacts on Oil Reservoirs), p. 77. Moscow: Nedra.
Taira, T.A., Nayak, A., Brenguier, F., Manga, M., 2018. Monitoring reservoir response to earthquakes and fluid extraction. Salton Sea Geotherm. field, California: Sci. Adv. 4 (1), e1701536.
Walsh, J.B., 1965. The effect of cracks on the compressibility of rock. J. Geophys. Res. 70 (2), 381–389.
Wennberg, O.P., Wall, B.G., Saether, E., Jounoud, S., Rozhko, A., Naumann, M., 2018, June. Fractures in chalks and marls of the shetland group in the gullfaks field, north sea. In: 80th EAGE Conference and Exhibition 2018, vol. 2018. European Association of Geoscientists & Engineers, pp. 1–5, 1.
Young, T., 1805. III. An essay on the cohesion of fluids. Phil. Trans. Roy. Soc. Lond. 95, 65–87.
Zare, K., Mahiyar, H., Ghaedi, M., 2021. Enhanced recovery from naturally fractured gas reservoirs with seismic vibrations. J. Energy Resour. Technol. 143 (3).
Zeng, C., Deng, W., Fan, W.J., Liu, K.H., 2020a. Investigation of the resonance of nonwetting droplets in constricted capillary tubes. Geophysics 85 (2). https://doi.org/10.1190/geo2019-0228.1. ID1–ID17.
Zeng, C., Deng, W., Fan, W.J., Liu, K.H., 2020b. "Reply to comments on "investigation of the resonance of nonwetting droplets in constricted capillary tubes" (chao Zeng, wen deng, jing fan, and kelly H. Liu, 2020, geophysics, 85, no. 2, 1D1–ID17),". Geophysics 85, X3–X5.
Zhang, B., He, Q., Lin, Z., Li, Z., 2021. Experimental study on the flow behaviour of water-sand mixtures in fractured rock specimens. Int. J. Min. Sci. Technol. 31 (3), 377–385.
Zhu, W., Wong, T.F., 1997. The transition from brittle faulting to cataclastic flow: permeability evolution. J. Geophys. Res. Solid Earth 102 (B2), 3027–3041.
Zimmerman, R.W., 1990. Compressibility of Sandstones, vol. 29. Elsevier.